



Universiteit
Leiden
The Netherlands

Mechanical metamaterials: nonlinear beams and excess zero modes

Lubbers, L.A.

Citation

Lubbers, L. A. (2018, September 13). *Mechanical metamaterials: nonlinear beams and excess zero modes*. *Casimir PhD Series*. Retrieved from <https://hdl.handle.net/1887/65383>

Version: Not Applicable (or Unknown)

License: [Licence agreement concerning inclusion of doctoral thesis in the Institutional Repository of the University of Leiden](#)

Downloaded from: <https://hdl.handle.net/1887/65383>

Note: To cite this publication please use the final published version (if applicable).

Cover Page



Universiteit Leiden



The handle <http://hdl.handle.net/1887/65383> holds various files of this Leiden University dissertation.

Author: Lubbers, L.A.

Title: Mechanical metamaterials: nonlinear beams and excess zero modes

Issue Date: 2018-09-13

2

A nonlinear beam model to describe the post-buckling of wide neo-Hookean beams

Wide beams can exhibit subcritical buckling, i.e. the slope of the force-displacement curve can become negative in the post-buckling regime. In this chapter, we capture this intriguing behaviour by constructing a 1D nonlinear beam model, where the central ingredient is the nonlinearity in the stress-strain relation of the beam's constitutive material. First, we present experimental and numerical evidence of a transition to subcritical buckling for wide neo-Hookean [52] hyperelastic beams, when their width-to-length ratio exceeds a critical value of 12%. Second, we construct an effective 1D energy density by combining the Mindlin-Reissner kinematics [41] with a nonlinearity in the stress-strain relation. Finally, we establish and solve the governing beam equations to analytically determine the slope of the force-displacement curve in the post-buckling regime. We find, without any adjustable parameters, excellent agreement between the 1D theory, experiments and simulations. Our work extends the understanding of the post-buckling of structures made of wide elastic beams and opens up avenues for the reverse-engineering of instabilities in soft and metamaterials.

The work presented in this chapter has been published as:

C. Coulais, J.T.B. Overvelde, **L.A. Lubbers**, K. Bertoldi and M. van Hecke, *Discontinuous buckling of wide beams and metabeams*, Phys. Rev. Lett. **115**, 044301 (2015).

L.A. Lubbers, M. van Hecke and C. Coulais, *A nonlinear beam model to describe the post-buckling of wide neo-Hookean beams*, J. Phys. Mech. Solids **106**, 191-206 (2017).

Guide through this chapter: Readers interested in the main findings can safely skip sections 2.3 to 2.5. These sections are very technical, but provide essential background information to unambiguously construct the energy density which forms the basis of our nonlinear beam model.

2.1 Introduction

Recent years have seen an upsurge of interest in the instabilities and post-instability behaviour of flexible structures. Rather than seeing instabilities as failure, they recently have been leveraged to achieve novel functional (meta)materials and structures [31, 53]. As such, materials and structures featuring snapping [44, 54], wrinkling [55, 56], fingering [57] or buckling [4, 36, 40] have been created. Collectively they constitute a promising route to develop mechanical devices for sensing [38, 58], actuation [55, 59–61] or soft robotics [62, 63].

These structures harness post-instabilities *and* their constituents undergo large deformations. A theoretical description of this regime, where as we will show nonlinearities are key, is not well developed yet. On the one hand, the description of post-buckling behaviour has been widely investigated, but for models in which the constitutive material is assumed to be linearly elastic under small deformations [30, 42, 43, 64–68]. On the other hand, much attention has been devoted to characterizing the instabilities of nonlinear elastic cellular materials [69–72] or structures [73], but only for the onset of instability, and not for the post-instability regime.

Euler buckling, known as the phenomenon where an elastic beam will buckle under a sufficiently large compressive axial load, is perhaps the simplest and the most widespread instability [24]. Much theoretical attention has been devoted to describing it using the classical [74, 75], extensible and shearable [76] elastica problem. Further in-depth studies have focused on the onset of buckling, the structure of buckled states [77, 78], closed form solutions [79–81], large deformations [82–84] and three-dimensional [85–88] deformations. In this chapter we investigate the post-buckling regime of wide beams, where strains are necessarily large. A salient feature of buckling of slender beams is that the post-buckling compliance increases tremendously after buckling, yet remains positive. However, as discussed in the general introduction of this thesis, wide beams that buckle and undergo large deformations can exhibit a negative

post-buckling compliance [40]. Although negative compliance is commonly observed in buckling of shells [30], pipes [64] and the wrinkling of membranes [89–91], it has not been reported for Euler beam buckling, and to the best of our knowledge is not predicted by existing beam models.

Here we develop a 1D nonlinear beam model based on a nonlinear constitutive equation, that without adjustable parameters, describes the post-buckling compliance of wide neo-Hookean beams. In particular, this model allows to analytically capture the onset of subcritical buckling (post-buckling slope < 0) for widths larger than approximately 15%, in good agreement with experiments and FEM simulations. First, in section 2.2 we present experimental and numerical evidence to show that for neo-Hookean beams, the post-buckling compliance becomes negative when the beam width-to-length ratio t exceeds approximately 12%. Second, in sections 2.3-2.5 we discuss the fundamental ingredients for our 1D model. We review mathematical beam descriptions based on Mindlin-Reissner kinematics [41], pinpoint and quantify the role of material nonlinearity using extensive 2D simulations, and construct a 1D energy density that encompasses such nonlinearity by combining the Mindlin-Reissner kinematics with a nonlinearity in the stress-strain relation. Third, in section 2.6 we establish the governing equations of our nonlinear 1D beam model that are based on this energy density including nonlinearity. We then solve the beam equations to obtain the variation of the post-buckling slope with t and find that, without any adjustable parameters, our model is in excellent agreement with experiments and simulations. Our work thus unambiguously unravels the link between stress-strain nonlinearity and post-buckling behaviour. While we focus on the buckling of wide neo-Hookean beams, we note that we only need to include quadratic corrections to the stress-strain relation to correctly capture the physics. Hence, for materials with other nonlinear constitutive laws, including metamaterials as explored in [40] and [92], our description is also valid. Our analytical description can be used to rationally design the post-buckling behaviour of beams, and we hope that it can inspire work to capture and describe post-instability behaviours of other elastic systems. More widely, our work may impact the design of compliant devices, which harness instabilities (e.g. buckling, snapping, wrinkling) to convey mechanical functionalities that are of use in soft robotics [62, 63], sensors [38, 58] and actuators [55, 59–61].

2.2 Phenomenology: Subcritical buckling

In this section, we present and expand the findings from our previous work on subcritical buckling of wide beams [40]. First, we discuss both the experimental and numerical protocols to study buckling of rectangular beams to determine the force-displacement relation. We consider both the numerical protocol for 3D FEM simulations with boundary conditions that closely model the experimental conditions, and 2D simulations with simplified boundary conditions. Second, we analyse the onset of buckling and the post-buckling compliance of beams of varying width-to-length ratio t . We then show that for both experiments and numerics the post-buckling compliance varies systematically with t , and becomes negative for $t \gtrsim 0.12$.

2.2.1 Experiments and FEM simulations

In the analysis below, we consider beams of the width-to-length ratio $t = w/\ell$ and depth d , under load F and corresponding uniaxial displacement u , where $u, F > 0$ correspond to a compressive deformation [Fig. 2.1(a-b)].

Experiments

To perform buckling experiments, we mold 12 solid rectangular beams of rest length $\ell = 45$ mm, depth $d = 35$ mm and widths ranging from $w = 1.55$ mm to $w = 12.85$ mm [Fig. 2.1(a)] out of a well-characterized silicon rubber (Zhermarck, Polyvinyl Siloxane double elite 8, density 1.15×10^3 kg/m³, Young's modulus $E = 250$ kPa, Poisson's ratio $\nu \approx 0.5$). The extremities of the beams are glued on plexiglass plates that are attached to the uniaxial testing device (Instron 5965) in order to approximate clamped-clamped boundary conditions, and we perform the experiments in a water bath in order to limit the effects of gravity.

3D simulations

We simultaneously carry out a nonlinear analysis using the commercial finite element package ABAQUS/STANDARD on beams with the exact same geometry as in the experiments. We determine the buckling point using a specific algorithm in our finite element code that does not require seeding

the initial geometry with imperfections (see appendix 2.A and reference [40]), allowing to obtain a 0.1% accuracy on the buckling onset.

Material model — The rubbers used in our experiments are well described by the incompressible neo-Hookean formulation of nonlinear elasticity [93]. We therefore use a neo-Hookean strain energy density [52] of the form

$$W = \frac{G}{2} \left(\det(\mathbf{F})^{-2/3} \text{tr}(\mathbf{F}\mathbf{F}^T) - 3 \right) + \frac{K}{2} (\det(\mathbf{F}) - 1)^2, \quad (2.1)$$

where G is the shear modulus, K the bulk modulus and $\mathbf{F} \equiv \partial\mathbf{x}/\partial\mathbf{X}$ is the deformation gradient tensor from the undeformed coordinates \mathbf{X} to the deformed coordinates \mathbf{x} . In the numerical analysis, we use the moduli $G = 83$ kPa and $K = 42$ GPa, which models accurately the $E = 250$ kPa nearly-incompressible rubber used in the experiments. We note that our results do not sensitively depend on the precise choice of G and K , as long as $G/K \ll 1$. The overall stiffness, given by the Young's modulus $E = 9KG/(3K + G)$, only sets a trivial scale, and to obtain dimensionless results, we scale the stresses by E for the results presented below.

Boundary conditions. — We numerically impose clamped-clamped boundary conditions to resemble the experiments where the endpoints of the beam are glued on plexiglass plates.

Simplified 2D FEM simulations

In addition, we carry out 2D plane stress simulations (Abaqus element type CPS4) using the same material model, yet with simplified slip boundary conditions at both endpoints of the beam, which allows for free lateral expansion at the clamped-clamped endpoints to avoid barrelling effects [94]. The choice for plane stress over plane strain conditions is a priori not obvious because our beams are intermediate between the plane stress limit ($w \gg d$), and plane strain limit ($w \ll d$). We therefore used our 3D simulations to investigate the 3D stresses and strains for beam thicknesses where the post-buckling slope changes sign ($t \approx 0.1$). We found that in this case there are significant out of plane strains, but that the out of plane stresses are small (ratio between the lateral and uniaxial stresses < 0.1) — this motivates us to focus on the plane stress case.

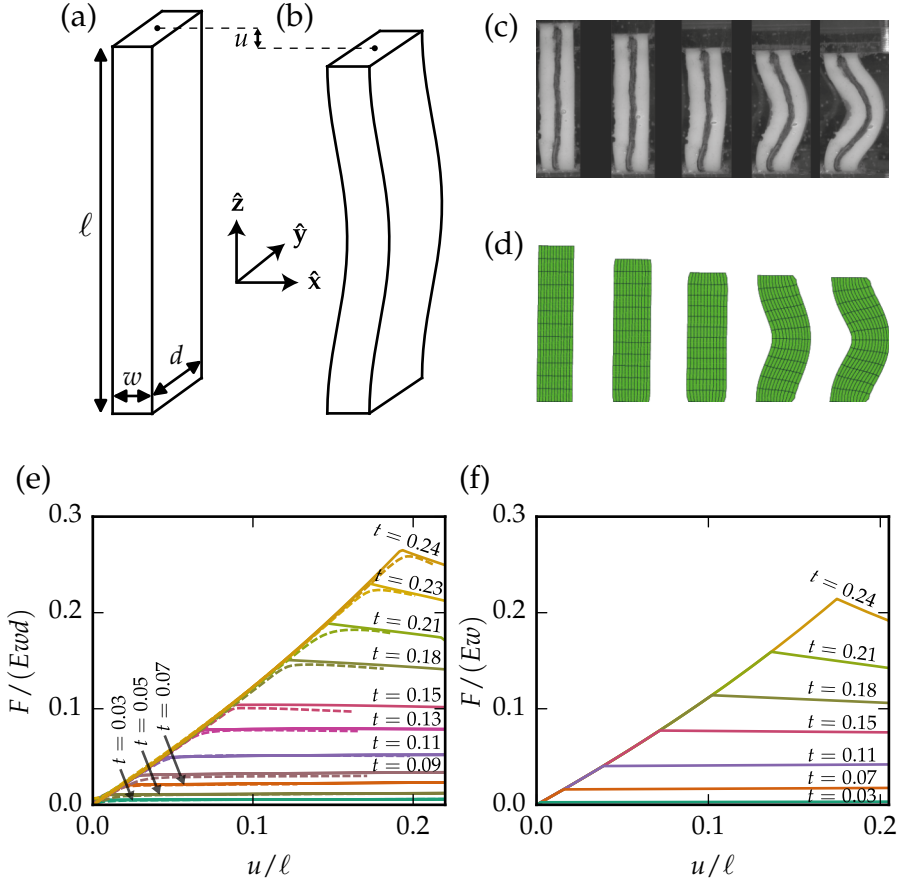


Figure 2.1: Buckling of wide neo-Hookean beams. (a) Sketch of a beam in its initial undeformed state, for which the beam has a rest length ℓ , width w and depth d . (b) Applying a compressive displacement u , leads to compression and eventually buckling of the beam. (c-d) Front-view snapshots of (c) the experiment and (d) the simulation for a beam of length $\ell = 45$ mm, depth $d = 35$ mm and width $w = 11.95$ mm, at compressive displacements (from left to right) $u = 0$, $u = 0.5 u_c$, $u = 0.99 u_c$, $u = 1.1 u_c$ and $u = 1.2 u_c$. (e-f) Scaled compressive force $F/(Ewd)$ vs. compressive displacement u/ℓ for beams of different width for (e) the experiments (dashed lines) and 3D simulations (solid lines) and (f) the simplified 2D simulations. As the effects of gravity are negligible in the experiments and absent in simulations, the choice of the Young's modulus E is irrelevant and we scale the forces by E .

The plane stress condition, which is nontrivial in finite-strain elasticity, is implemented by requiring that the yy -component [Fig. 2.1(a)] of the true (Cauchy) stress is zero, which necessitates the iterative computation of the deformation gradient component F_{yy} to satisfy this condition [95]. Altogether, these assumptions ensure that more complex 3D and boundary effects can be neglected and allow us to carry out the analysis in the simplest setting where subcritical buckling can be observed, and will be used later to pinpoint the physical mechanism at stake in the post-buckling behaviour of wide beams.

2.2.2 Buckling and Subcritical Buckling

In Fig. 2.1(c-d) we simultaneously display 5 front-view snapshots of experiments and 3D simulations for a beam with $t = 0.23$ ($w = 10.20$ mm) at different compressive displacements, which are in very good qualitative agreement. Moreover, we plot the obtained force-displacement curves for the complete range of beam widths in Fig. 2.1(e), which illustrates that 3D simulations and experiments are also in very good quantitative agreement. Hence, the neo-Hookean material model describes the buckling of wide beams well. For all curves, we observe a near-linear increase until the onset of buckling, at which the slope abruptly changes. For thin beams, the force increases after buckling, while for thick beams, the force decreases. For buckling experiments under controlled force of a sufficiently wide beam, the post-buckling branch would thus be unstable and the pitchfork instability would be subcritical. Therefore, we refer to this type of instability as *Subcritical Buckling*. The 2D simulations, albeit considerably simpler, display qualitatively similar behaviour [Fig. 2.1(f)], which demonstrates that subcritical buckling does originate neither from boundary-induced singularities nor from 3D effects. To the best of our knowledge, although subcritical buckling is fairly common in other settings such as the wrinkling instability [96–98] and the wrinkle-to-fold transition [89–91], such sign change is not predicted by any theory as of now for the Euler buckling of wide beams for realistic aspect ratios. Note that Magnusson et al. [42] predicted such transition from supercritical to subcritical post-buckling, yet for overly large aspect ratios ($t=0.24$), and for which the validity of the extensible, non-shearable elastica is not guaranteed.

We now retrieve the onset of buckling u_c and the post-buckling slope

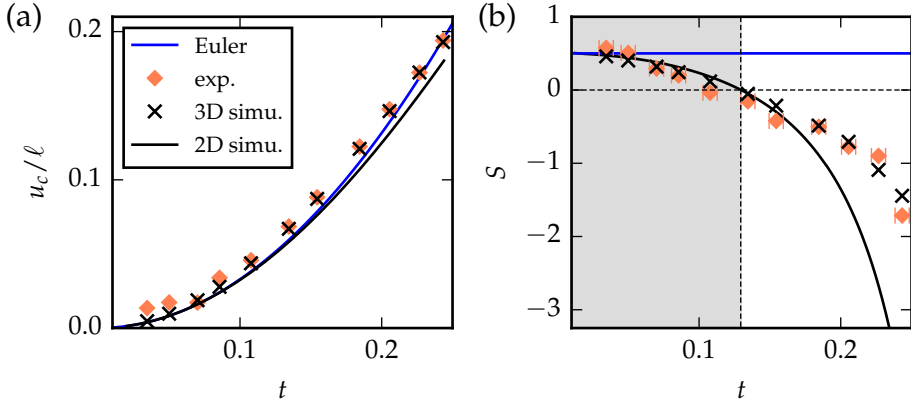


Figure 2.2: Critical compressive displacement and post-buckling slope as function of the beam width-to-length ratio, for Euler's elastica (solid blue), experiments (orange diamonds), 3D FEM simulations (black crosses) and 2D plane stress FEM simulations (solid black). (a) The onset of buckling, u_c , in experiments and simulations qualitatively follows Euler's elastica. (b) The post-buckling slope S in experiments and simulations progressively deviates from the Euler limit $S = 1/2$ for large t . The transition to subcritical buckling ($S < 0$) occurs for $t \gtrsim 0.12$, as indicated by the shaded region.

S , using the relation between the load F and the compressive displacement u in the post-buckling regime:

$$\frac{F - F_c}{F_c} = S \frac{(u - u_c)}{\ell} + \mathcal{O}\left(\left(\frac{u - u_c}{\ell}\right)^2\right), \quad (2.2)$$

with F_c the critical buckling force. In Fig. 2.2(a) we display the onset of buckling as a function of the beam width-to-length ratio t , for the experiments, 3D FEM simulations and the 2D FEM simulations, and observe quantitative agreement with the prediction of Euler's elastica for clamped-clamped boundary conditions, $u_c^{euler}/\ell = t^2\pi^2/3$ [30]. While the onset shows quantitative agreement with Euler's prediction, the results in Fig. 2.2(b) show that the post-buckling slope S strongly deviates from Euler's prediction $S = 1/2$ as t increases, and becomes *negative* for $t \gtrsim 0.12$. Importantly, Fig. 2.2(b) illustrates that subcritical buckling of wide beams is a robust phenomena: Even with the simplifications made in the 2D simulations, the differences in the post-buckling slope between 2D and 3D simulations are modest.

The emergence of subcritical Euler buckling is, as we will show, readily related to nonlinearity in the stress-strain relation [40]. In the following, we will rationalize this behaviour of wide beams—which are 3D structures undergoing large deformations—by constructing a 1D beam model that encompasses such a stress-strain nonlinearity. The behaviour of such a 1D model is more easily tractable than a full tensorial description needed in 3D, and is therefore of significant interest for the design of post-instabilities.

In conclusion, we have shown in this section that, in experiments, in fully 3D numerical simulations, and in 2D simulations, the post-buckling compliance of wide beams varies systematically with the beams aspect ratio t , and becomes negative for $t \gtrsim 0.12$.

Sections 2.3-2.5 provide technical information about the ingredients of our nonlinear 1D beam model. In subsequent order, we review mathematical descriptions of beams, pinpoint and quantify material nonlinearity using extensive 2D simulations and construct a 1D energy density encompassing such nonlinearity. As mentioned before, the reader interested in the main findings of this chapter can continue to section 2.6.

2.3 Mathematical description of beams

In this section we review the basic ingredients and assumptions for 1D beam models of varying degree of sophistication [24, 42, 43]. First, we discuss how 2D deformations of (wide) beams can be mapped onto the deformations of a 1D central beam axis, using the Mindlin-Reissner kinematics [41], which captures the extension, shear and bending of wide beams. Second, we review the governing beam equations that follow from the combination of Mindlin-Reissner kinematics and a linear constitutive law. Third, we numerically solve the most sophisticated linear beam model and compare its outcome to our 2D FEM results in the post-buckling regime. We find that for wide beams, this linear model does not accurately capture the beam shape. These deviations imply that nonlinear corrections to the constitutive law must be taken into account.

2.3.1 Mindlin-Reissner kinematics and strains

We now introduce the Mindlin-Reissner beam kinematics and associated strains that form the basis of our 1D beam description, presented later in this chapter.

The buckling regime of slender beams (elastic lines, $t \rightarrow 0$) is bending dominated. Therefore, their shape can be described by a single kinematic field, denoted $\theta(s)$ [Fig. 2.3(a)], which is the rotation angle with respect to the z -axis as a function of the curvilinear coordinate s along the beam [99]. Wide beams, however, have additional modes of deformation, which are dominantly compressive and shear deformations. Following [41, 43, 100], the shape of such beams can be captured by a central beam axis described by a deflection and shear angle, respectively defined as $\theta(s)$ and $\chi(s)$, along with the stretch $\lambda(s)$ [Fig. 2.3(c)]. We refer to this kinematic description as *Mindlin-Reissner kinematics*. The stretch along the central axis is defined as the elongation of a beam element of length ds in the undeformed state, with respect to the same element in the deformed state of length ds' , that is, $\lambda(s) = ds'/ds$. Furthermore, the sum of the rotation angle and shear angle, $\theta(s) + \chi(s)$, is defined as the angle enclosed by the vertical vector \mathbf{e}_z and the tangent to the central axis, \mathbf{t} . The shear angle can be regarded as the angle enclosed within the normal of the central axis, \mathbf{n} , and the tangent to the deformed cross-section in the vicinity of the central axis, \mathbf{n}' [zoomed area in Fig. 2.3(c)]. The rotation angle can then readily follow from the difference between the sum $\theta(s) + \chi(s)$, and $\chi(s)$ itself. Following [41], the Mindlin-Reissner kinematics can be used to introduce a set of compressive, bending, and shear strains, respectively denoted $\tilde{\varepsilon}_0$, ε_1 and γ_0 , and defined as

$$\tilde{\varepsilon}_0 = \lambda \cos(\chi) - 1, \quad (2.3)$$

$$\varepsilon_1 = \theta_s, \quad (2.4)$$

$$\gamma_0 = \lambda \sin(\chi). \quad (2.5)$$

In the reminder of this chapter, we refer to this set of strain-displacement relations as the *Mindlin-Reissner strains*. In order to obtain a set of closed beam equations, these strains should be related to stresses via constitutive relations. In the following section we review prior (wide) beam models that are constructed from a combination of Mindlin-Reissner strains and linear elasticity.

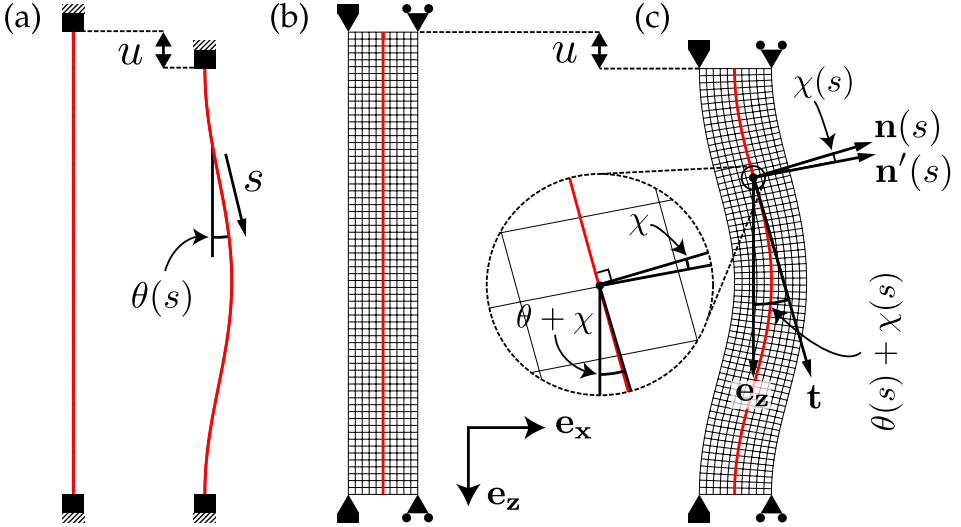


Figure 2.3: Kinematic description of a slender ($t = 0^+$) and wide beam (here, $t = 0.15$). Both beams are compressed equally by a displacement u . (a) The shape of an undeformed (left) and buckled (right) slender beam. We obtain the buckled state by solving Euler's elastica [Eq. (2.6)] for clamped boundary conditions at both ends. The kinematic description of a slender beam is governed by the rotation angle $\theta(s)$. (b) Snapshot from a 2D simulation of a wide neo-Hookean beam in its undeformed state, where each square represents a simulation element. We impose clamped boundary conditions at both ends of the beam, but allow free lateral expansion along the x -direction at top and bottom boundaries. The superimposed, red, solid line depicts the central axis of the beam as obtained from FEM simulations accordingly. (c) Snapshot from the same simulation as in (b), depicting the beam in its deformed state. The deflection of the central axis under a compressive displacement u is described by a combination of the rotation angle, $\theta(s)$, and shear angle, $\chi(s)$ along the curvilinear coordinate of the beam as indicated. For a precise definition of $\theta(s)$ and $\chi(s)$ as well as the vectors $\mathbf{n}(s)$, $\mathbf{n}'(s)$ and $\mathbf{t}(s)$, see the main text.

2.3.2 Linear beam models

Here we present a number of existing models that combine the Mindlin-Reissner strains with conventional *linear* elasticity. We start with a brief review of the bending of elastic lines (Euler's elastica), followed by more complete models that include extensibility and shear effects [42, 43].

Euler's limit— Slender beams can be described through a single Mindlin-Reissner strain, θ_s . The governing beam equation to be satisfied by the bending strain then reads [30]:

$$EI\theta_{ss} + F\sin\theta = 0, \quad (2.6)$$

where I is the second moment of area, which equals $I = \frac{1}{12}w^3d$ in case of the rectangular cross-section of width w and depth d considered here. The above equation is formally known as Euler's elastica and can be solved analytically to provide an exact prediction for the critical buckling force [99].

Euler's elastica rests on two assumptions, which are of importance as they help us to understand where wide beams start to deviate from slender beams. First, within the reference frame defined in Fig. 2.3(b), the elastica tacitly assumes that the axial nominal strain ε_{zz} across the beam is given by

$$\varepsilon_{zz}(x) = \varepsilon_1 x, \quad (2.7)$$

where x is the horizontal coordinate across the beam section and ε_1 is the curvature of the central axis of the beam, as defined by Eq. (2.4). Second, it assumes a linear constitutive relation between the axial nominal stress σ_{zz} and axial nominal strain, that is,

$$\sigma_{zz} = E\varepsilon_{zz}. \quad (2.8)$$

This assumption of linear elasticity is common regarding slender beams and provides an excellent description of their buckling properties, because the typical strains involved in slender beam buckling are much smaller than unity, $u_c/\ell \ll 1$.

Shearable and extensible beams — Wide beams necessitate the use of all three Mindlin-Reissner strains due to additional compressive and shear deformations. Consequently, the governing beam equations now constitute a set of three coupled equations, rather than a single equation in the case of slender beams. Since the strains involved in wide beam buckling can be substantial (*e.g.* $\sim 10\%$ for a beam with $t = 0.17$), nonlinearities in the stress-strain relation induced by large deformations become significant. Nonetheless, as a first step, recent work [43] has combined all

three Mindlin-Reissner strains with linear elasticity,

$$EI\theta_{ss} + F((1 + \tilde{\epsilon}_0)\sin\theta + \gamma\cos\theta) = 0, \quad (2.9a)$$

$$EA\tilde{\epsilon}_0 + F\cos\theta = 0, \quad (2.9b)$$

$$GA\gamma + F\sin\theta = 0, \quad (2.9c)$$

where, $A = wd$ is the cross-sectional area. In the remainder of this manuscript we refer to the above set of equations as the *linear beam model*. Note that previous work also considered beam models that take into account exclusively bending and shear [100, 101] deformations, known as Timoshenko beams, or solely bending and extensibility [42].

As we will show later in section 2.6, the linear beam model somewhat improves the post-buckling description in comparison to Euler's elastica ($S = 1/2$), but fails to predict the experimentally and numerically observed subcritical buckling. Specifically, in the following section we illustrate that the strains predicted by the *linear* elastic beam model significantly deviate from the strains obtained by the 2D FEM simulations, already for a beam of width-to-length ratio $t = 0.1$. This evidences that the Mindlin-Reissner strains given by Eqs. (2.3-2.5) —which remain valid for large strains [85]— cannot be accurately determined from a closed set of beam equations based on linear elasticity. Instead, to accurately predict the post-buckling slope and Mindlin-Reissner strains from a set of beam equations, one needs to develop a model that takes into account a non-linear stress-strain relation, which is the main objective of this chapter.

2.3.3 Linear wide beam model compared to 2D FEM simulations

We now compare the Mindlin-Reissner strains predicted by the linear beam model [Eqs. (2.9)] to our results obtained from the 2D FEM simulations (Fig. 2.4). Using a shooting method in *Mathematica*, we solve numerically the linear beam model, with boundary conditions $\theta(0) = 0$ and $\theta_s(0) = \theta_s(1) = C$, where C is a constant directly set by the amount of uniaxial displacement u . Comparing the results from FEM simulations (solid black lines) in Fig. 2.4(a-c) with those of the linear beam model, we observe a qualitative agreement for bending and shear deformations. However, there is a very striking difference between the model predictions and numerical results for the compressive deformations [Fig. 2.4(a)]:

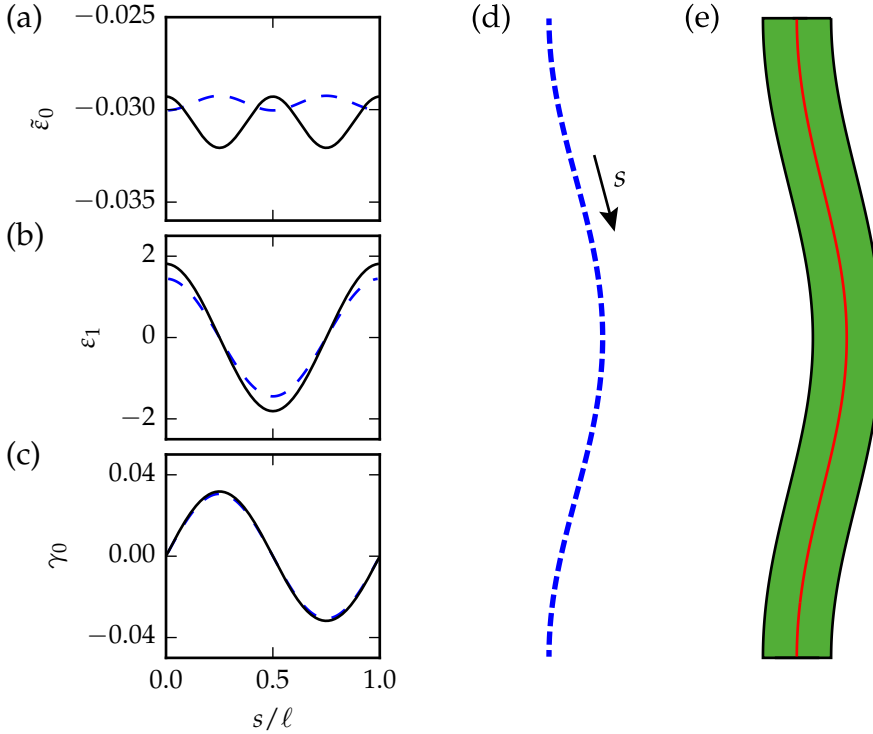


Figure 2.4: Mindlin-Reissner strains and corresponding beam shapes for a beam ($t = 0.1$) which is uniaxially compressed to a displacement of $u/u_c = 1.3$. (a–c) The solid black curves depict data for the Mindlin-Reissner strains obtained from FEM simulations, and the blue dashed curves are numerical solutions of the linear elastic wide beam model [Eqs. (2.9)]. As a function of the curvilinear coordinate s , we show (a) the compressive strain, (b) the bending strain, and (c) the shear strain. (d) Shape of the central axis as predicted by the linear beam model. We have obtained this shape by the integration of the horizontal and vertical component of the displacement gradient with respect to s , respectively given by $\lambda \cos(\theta + \chi)$ and $\lambda \sin(\theta + \chi)$ [41]. (e) Beam shape and associated central axis (solid red) obtained from 2D FEM simulations.

the actual (numerical) modulations of the stretch are much stronger, and incidentally are opposite, to those predicted by the model. Subtle as this deviation may be, the linear beam model cannot predict the experimentally and numerically subcritical buckling (see section 2.6). This suggests that this subtle deviation points to a more fundamental flaw of the linear

model, which arises due to the large deformations that are unavoidable in wide-beam buckling. In the following sections we will uncover, clarify and model the role of nonlinearity in the constitutive equation as the crucial ingredient to describe the post-buckling regime of wide beams.

2.4 Quantifying the role of material nonlinearity

In this section we use FEM simulations to disentangle nonlinearities in the relation between nominal stress and strain. We focus on a transversal slice across the middle of the beam, obtain the stress and strain profiles for slender and for wide beams, both close to and deep into the post-buckling regime. These profiles unambiguously show that, for thick beams, axial stresses and strains are no longer linearly related, but that rather a neo-Hookean description, where the stress is a nonlinear function of strain, describes the data with high accuracy, for beam aspect ratios up to $t \approx 0.2$ and for compressions up to 115% of the critical compression where buckling takes place. We then quantify these axial nonlinearities by a systematic powerlaw expansion of the nominal strain and stress as function of the lateral coordinate, thickness and compression. The leading order terms in this expansion are consistent with Euler's *Elastica*, but it is not a-priori clear what the structure of the higher order terms is. We therefore use our FEM data to determine the leading order terms in this expansion. This numerical input circumvents the need for heuristics to guess the important terms, and leads to a greatly simplified model where the dominant next order terms in t are properly taken into account. As we will show, these next order terms evidence a nonlinearity in the stress-strain relation which is consistent with the material nonlinearity of neo-Hookean materials [52]. Finally, we repeat the above analysis for the nominal shear strain and stress and show that shear strain and stress can be related linearly. Hence, the crucial main missing ingredient in the linear elastic wide beam model is nonlinearity in the axial nominal strain and stress relation.

2.4.1 Nonlinear uniaxial transverse stress and strain profiles

We start by considering the shape of the transverse profiles of the axial nominal strain, ε_{zz} , and stress, σ_{zz} . We restrict our attention to the cross-

section at the middle of the beam, depicted by the horizontal red lines in Fig. 2.5(a-b). We found (not shown) that the discrepancy between the observed and predicted sinusoidal modulation of $\tilde{\varepsilon}_0$, identified in Fig. 2.4(a), is maximal at the middle of the beam in the immediate post-buckling regime. We then consider $\varepsilon(x) \equiv \varepsilon_{zz}(x, s = \ell/2)$ and $\sigma(x) \equiv \sigma_{zz}(x, s = \ell/2)$ to measure the spatial shape of the axial nominal strain and stress as a function of the transverse coordinate, x , of the deformed geometry.

In the pre-buckling regime, the uniaxial nominal stresses and strains are simply constants as function of x as the beam undergoes uniform uniaxial compression. Under uniaxial uniform compression the neo-Hookean relation predicts the following nominal stress-strain relation (see appendix 2.B.1)

$$\sigma_{nH}(x) = \frac{E}{3} \left(1 + \varepsilon - \frac{1}{(1 + \varepsilon)^2} \right). \quad (2.10a)$$

The nonlinearity of this stress-strain relation stems from the combination of large deformations and incompressibility. This nonlinearity can qualitatively be understood from the fact that upon compression (tension) the cross-sectional area increases (decreases) and the stress-strain curve is therefore effectively stiffening (softening). The above equation can be expanded for small strain, ε , as

$$\sigma_{nH}(x) = E (\varepsilon - \varepsilon^2) + \mathcal{O}(\varepsilon^3). \quad (2.10b)$$

Hence, the linear term is consistent with Hookean elasticity and the leading nonlinear term is quadratic.

In contrast to the uniform uniaxial deformations considered above, buckled beams experience non-uniform deformations, and spatially varying stress and strain fields. Therefore we focus in the following on the evolution of the stress and strain profiles as the excess displacement Δu in the post-buckling regime is increased. In Fig. 2.5 we have plotted the nominal stress rescaled by the Young's modulus (solid black) and nominal strain profiles (dashed red) as function of x in the post-buckling regime, for a slender ($t = 0.01$) and wide ($t = 0.15$) beam.

For slender beams, the strains remain sufficiently small for the linear stress-strain relation to be valid. First, in Fig. 2.5(c) we demonstrate that the slender beam at small excess displacement has linear nominal stress

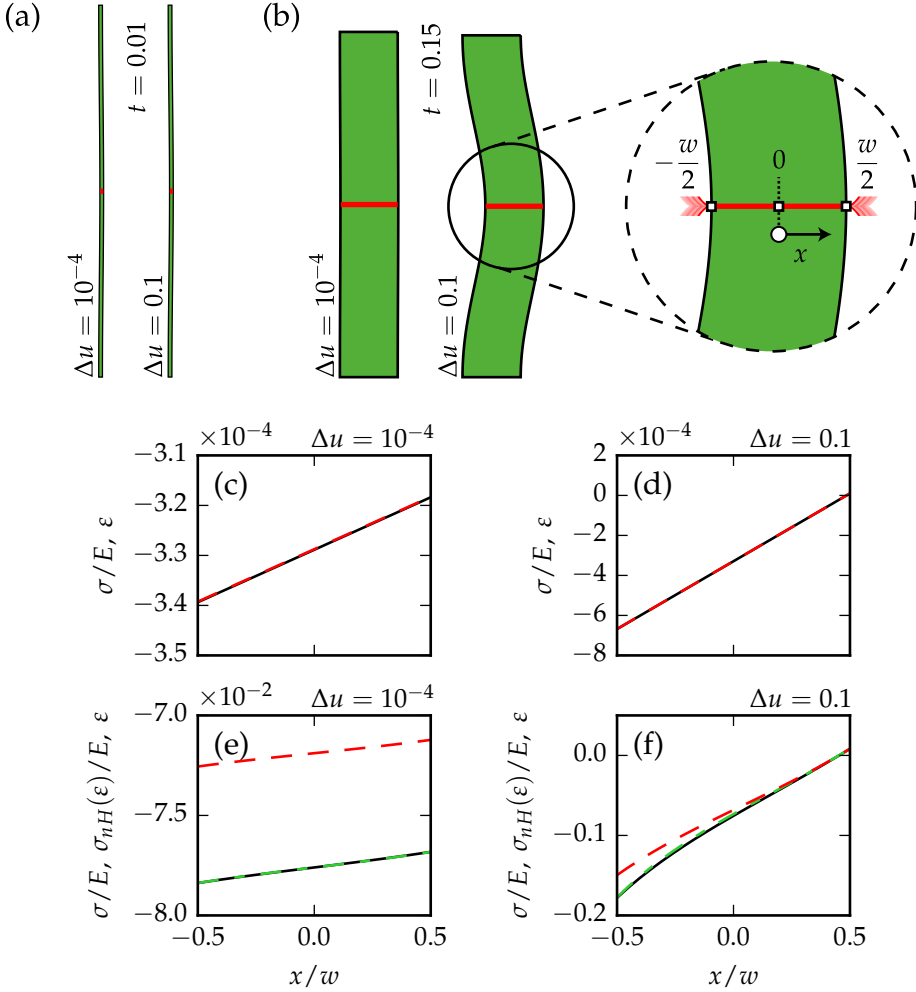


Figure 2.5: Beam shapes, stress-strain relation and stress and strain profiles. (a-b) Beam shapes for (a) a slender ($t = 0.01$) and (b) wide ($t = 0.15$) beam at excess strains of $\Delta u = 1 \times 10^{-4}$ and $\Delta u = 0.1$. We track the nominal stress and strain profiles as a function of the transverse coordinate x at the central cross section of the beam, depicted by the horizontal red lines. (c-d) Rescaled uniaxial nominal stress (solid black) and strain (dashed red) profiles for a slender beam ($t = 0.01$) at an excess strain of (c) $\Delta u = 1 \times 10^{-4}$ and (d) $\Delta u = 0.1$. (e-f) Rescaled uniaxial nominal stress and strain profiles for a wide beam ($t = 0.15$) at an excess strain of (e) $\Delta u = 1 \times 10^{-4}$ and (f) $\Delta u = 0.1$. The green dash-dotted lines correspond to $\sigma_{nH}(\epsilon)/E$, obtained by applying the neo-Hookean stress-strain relation in Eq. (2.10a) to the strain profile obtained from FEM simulations.

and strain profiles across the beam, and that $\sigma/E = \varepsilon$ is a very good approximation. In panel (d) we show data for $\Delta u = 0.1$, which results in a larger average nominal strain and a larger range of nominal strains across the beam, but the profiles remain linear and $\sigma/E \approx \varepsilon$. Both panel (c) and (d) show that the nominal strains involved in slender beam buckling remain sufficiently small for the nominal stress and strain to be simply proportional, as $\sigma = E\varepsilon$. Hence, the stress-strain nonlinearity is negligible for slender beams, both at small (panel c) and larger (panel d) excess displacement.

In contrast to slender beams, nonlinearities become important for thick beams. In Fig. 2.5(e-f) we have plotted the nominal stress and strain profiles for a wide beam ($t = 0.15$) at $\Delta u = 1 \times 10^{-4}$ and $\Delta u = 0.1$. For small excess displacement, $\Delta u = 1 \times 10^{-4}$, the nominal stress and strain profiles are both linear, but $\sigma/E \neq \varepsilon$. This is because the strains involved are sufficiently large for the neo-Hookean nonlinearity to become important. Indeed, when calculating $\sigma_{\text{NH}}(\varepsilon)$ from Eq. (2.10a), using the numerically obtained strain profile, we find that this stress describes the data extremely well (green dash-dotted curve). For larger excess displacement ($\Delta u = 0.1$), the effect of the nonlinearity is even more pronounced. We note that here a large range of strain occurs, and that the stress profile becomes strongly nonlinear in x . Again, using the nonlinear stress-strain relation in Eq. (2.10a), $\sigma_{\text{NH}}(\varepsilon)$ describes the numerical stress data very accurately. Taken together, our FEM data provides strong evidence that to correctly describe the stresses in thick beams in the post-buckling regime, including the neo-Hookean correction is necessary and sufficient.

2.4.2 Series expansion of the axial nominal stress and strain

In this section we perform a systematic polynomial expansion of the nominal stress and strain profiles in x/w , t and Δu , and determine all prefactors and scaling exponents using our FEM results. Our findings are consistent with the Euler limit at lowest order in t (quadratic) and confirm that stress and strain are nonlinearly related for higher order in t (quartic and higher).

Polynomial expansion and asymptotic analysis

As described above, the data in Fig. 2.5 suggests that the nominal stress and strain profiles are linear in x for (i) small t or (ii) small Δu , but become nonlinear when t and Δu are large. It is then natural to expand the nominal strain and stress around the buckling strain and stress, respectively denoted ε_b and σ_b , as function of the (scaled) transverse coordinate x/w :

$$\varepsilon\left(t, \Delta u, \frac{x}{w}\right) - \varepsilon_b = \sum_{n=0} C_n(t, \Delta u) \left(\frac{x}{w}\right)^n, \quad (2.11a)$$

and

$$\frac{\sigma - \sigma_b}{E} \left(t, \Delta u, \frac{x}{w}\right) = \sum_{n=0} D_n(t, \Delta u) \left(\frac{x}{w}\right)^n, \quad (2.11b)$$

where C_n and D_n are the coefficients of the expansion in x/w of order n . In the remainder of this manuscript, we will refer to these coefficients as the *post-buckling profile coefficients*. At buckling ($\Delta u = 0$), $C_n = D_n = 0$, so it is natural to assume that the post-buckling profile coefficients C_n and D_n grow as power laws in t and Δu in the post-buckling regime. Therefore, we postulate:

$$C_n(t, \Delta u) = \bar{C}_n t^{\alpha_n} \Delta u^{\beta_n}, \quad (2.12a)$$

and

$$D_n(t, \Delta u) = \bar{D}_n t^{\rho_n} \Delta u^{\tau_n}. \quad (2.12b)$$

Here, α_n , β_n , ρ_n and τ_n are *post-buckling profile scaling exponents* and \bar{C}_n and \bar{D}_n are the *post-buckling profile prefactors* which we will now determine up to the order $n = 5$ from our numerical simulations. Because of the nature of the Euler buckling instability, we expect that the exponents β_n and τ_n for all value of n will be half integers. Furthermore, as nominal stress and strain are linearly related in lowest order, stress and strain expansions should have the same post-buckling profile scaling exponents with t and Δu for every order, that is $\alpha_n = \rho_n$ and $\beta_n = \tau_n$. We also notice that the order $n = 1$ corresponds to the post-buckling stress and strain profiles of Euler's elastica, for which the post-buckling profile coefficients C_1 and D_1

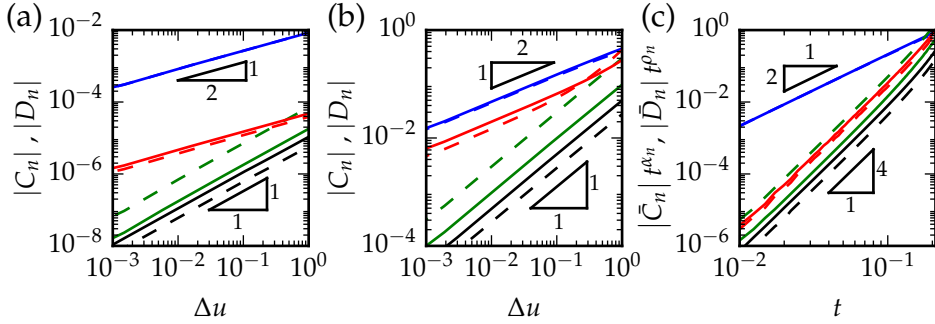


Figure 2.6: Expansion of the nominal strain and stress profiles obtained by FEM simulations, according to Eqs. (2.11-2.12). We plot the post-buckling profile coefficients C_n and D_n in each order as a function of Δu and t . In black, blue, green and red we have plotted C_n (solid lines) and D_n (dashed lines), corresponding to the order $n = 0, n = 1, n = 2$ and $n = 3$ respectively. (a-b) We have plotted $|C_n|$ and $|D_n|$ as function of Δu for a (a) slender beam ($t = 0.02$) and (b) thick beam ($t = 0.15$). (c) Dependence of C_n and D_n on the beam's aspect ratio t .

can be calculated analytically; below we find that the numerical results for C_1 and D_1 are consistent with their analytical predictions.

To determine all the constants, we use the numerical protocol described in section 2.2.1 and perform $N = 10^2$ simulations for beams with a logarithmically spaced width-to-length ratio in the range from $t = 0.01$ up to $t = 0.25$, and with an excess strain that is increased from $\Delta u = 10^{-3}$ up to $\Delta u = 1$ in 3×10^2 subsequent steps. For each simulation we extract the spatial shape of the nominal stress and strain as function of x/w across the middle of the beam at $s = \ell/2$ and fit $\varepsilon(x)$ and $\sigma(x)/E$ to polynomials of order $n = 5$, by which we obtain the post-buckling profile coefficients $C_n(t, \Delta u)$ and $D_n(t, \Delta u)$ for each specific set of parameter values t and Δu .

One subtle point is that such powerlaw fits are very sensitive to the determination of the point $\Delta u = 0$. To accurately determine Δu , we need an accurate measurement of the critical displacement u_c , as Δu and u_c are related through $\Delta u = u/u_c - 1$. The numerical estimation, u_c^n , determined in FEM simulations through the nonlinear buckling analysis, typically has a relative error of 10^{-3} which is not sufficient when considering the scaling near the critical point. Therefore, we correct $u_c = u_c^n - 1 + \delta$, where the correction δ ensures an increased accuracy for Δu . For each beam we have determined δ from fitting Eq. (2.13a) to our numerical data for C_1 .

We choose $n = 1$ to determine Δu , because the linear order is the most pronounced (Fig. 2.6) and therefore gives the most accurate measurement of δ . Having determined δ for $n = 1$, we subsequently fix δ to the same value for $n = 0, 2, 3, 4, 5$.

Scaling of the coefficients C_n and D_n with Δu

In this section we describe the scaling of the post-buckling profile coefficients C_n and D_n with Δu for fixed t , i.e., we determine the post-buckling profile exponents β_n and τ_n . In Fig. 2.6(a-b) we plot the coefficients C_n and D_n as function of Δu , for fixed t . In panel (a) and (b) we show results for a slender ($t = 0.02$) and wide ($t = 0.15$) beam, respectively. To uncover power law behaviour for Δu in C_n and D_n we use a log-log scale and then plot $|C_n(\Delta u)|$ (solid lines) and $|D_n(\Delta u)|$ (dashed lines). Note that both panels show results up to $n = 3$ — for higher order terms the scaling exponents and prefactors are provided in Tables (2.1-2.2)). From the straight lines on the log-log scale in Fig. 2.6(a-b) it becomes apparent that C_n and D_n show power law behaviour in Δu as was postulated already in Eqs. (2.12).

Fitting protocol — To determine the post-buckling profile scaling exponents, β_n and τ_n , we first take the absolute sign and log on both sides of Eqs. (2.12) which yields

$$\log(|C_n|) = \beta_n \log(\Delta u) + \log[|\bar{C}_n| t^{\alpha_n}], \quad (2.13a)$$

and

$$\log(|D_n|) = \tau_n \log(\Delta u) + \log[|\bar{D}_n| t^{\rho_n}], \quad (2.13b)$$

and then fit our numerical data for the post-buckling profile coefficients C_n and D_n to their respective equations as given directly above. We have tabulated the scaling exponents β_n and τ_n in Table 2.1 up to $n = 5$.

Results — With a fitting range for Δu in $[10^{-3}, 10^{-1}]$ at fixed t , we measure identical exponents for nominal stress and strain within their error bars: $\beta_0 = \tau_0 \approx 1.0$ [black lines in Fig. 2.6(a-b)], $\beta_1 = \tau_1 \approx 0.5$ (blue lines), $\beta_2 = \tau_2 \approx 1.0$ (red lines), and $\beta_3 = \tau_3 \approx 0.5$ (green lines). This is consistent with our earlier assertion that these exponents can be expected

n	Δu		t	
	β_n	τ_n	α_n	ρ_n
0	1.03 ± 0.1	1.05 ± 0.1	4.06 ± 0.4	4.09 ± 0.4
1	0.51 ± 0.03 [$\frac{1}{2}$]	0.51 ± 0.03 [$\frac{1}{2}$]	2.00 ± 0.1 [2]	1.99 ± 0.1 [2]
2	1.03 ± 0.1	1.02 ± 0.1	4.02 ± 0.4	4.00 ± 0.4
3	0.51 ± 0.05	0.51 ± 0.05	4.00 ± 0.4	3.99 ± 0.4
4	1.0 ± 0.15	1.01 ± 0.15	6.05 ± 0.9	6.00 ± 0.9
5	0.51 ± 0.15	0.52 ± 0.16	6.20 ± 1.9	5.82 ± 1.7

Table 2.1: Post-buckling profile scaling exponents of Δu and t , for the expansion of the nominal strain and stress profiles as defined in Eqs. (2.11-2.12). Each row corresponds to a different order of n and values within the square brackets represent analytical results as predicted by Euler’s elastica. The error in the relevant scaling exponents is an estimation which we assign to a combination of uncertainties: (i) The error in Δu , which is particularly important for the scaling near the critical point; (ii) The finite range of Δu and t over which the scaling holds is at most 2 decades; (iii) The quantities $\bar{C}_n t^{\alpha_n}$ and $\bar{D}_n t^{\alpha_n}$, necessary to determine the scaling exponents for t , are obtained by extrapolating C_n and D_n to $\Delta u = 1$ [Eqs. (2.13)], hence this error propagates when determining the scaling exponents for t . Taking all effects into account, we estimate an fitting error of 5% for $n = 1$, 10% for $n = 0, 2, 3$, 15% for $n = 4$ and 30% for $n = 5$.

to be half-integers, and we will now assume they are. As we will further discuss in the following, while the $n = 1$ term dominates for slender beams [Fig. 2.6(a)] and corresponds to Euler’s elastica, other orders $n \neq 1$ become significant for wider beams [Fig. 2.6(b)].

Scaling of the coefficients C_n and D_n with t

The next step is to determine how the post-buckling profile coefficients C_n and D_n scale with the beam’s aspect ratio t , hence determining the post-buckling profile exponents α_n and ρ_n .

Fitting protocol — The first step is to refine the fit of Eqs. (2.13) to our numerical data for C_n and D_n . To do so, we fix the post-buckling profile exponents β_n and τ_n to their nearest half integer values, which results in alternating exponents 1 or 1/2: $\beta_0 = \tau_0 = 1$, $\beta_1 = \tau_1 = 1/2$, $\beta_2 = \tau_2 = 1$,

and so on. This procedure reduces the number of fitting parameters and thus provides a more accurate measure of the constants $\log[\bar{C}_n t^{\alpha_n}]$ and $\log[\bar{D}_n t^{\rho_n}]$, where t is held fixed in this fitting procedure. By repeating this analysis for t in the range $[10^{-2}, 0.25]$, we determine the constants $\bar{C}_n t^{\alpha_n}$ and $\bar{D}_n t^{\rho_n}$ for each t and plot them versus t on a log-log scale in Fig. 2.6(c). Obviously, the straight lines in Fig. 2.6(c) on the log-log scale suggest that C_n and D_n show power law behaviour in t as well. Fitting this data to

$$\log(|\bar{C}_n| t^{\alpha_n}) = \log(|\bar{C}_n|) + \alpha_n \log(t), \quad (2.14a)$$

and

$$\log(|\bar{D}_n| t^{\rho_n}) = \log(|\bar{D}_n|) + \rho_n \log(t), \quad (2.14b)$$

with t in the range $[10^{-2}, 10^{-1}]$. An overview of the scaling exponents α_n and τ_n up to order $n = 5$ is provided in Table 2.1.

Results — We measure identical post-buckling profile exponents for stress and strain within their error bars: $\alpha_0 = \rho_0 \approx 4.0$ (black lines), $\alpha_1 = \rho_1 \approx 2.0$ (blue lines), $\alpha_2 = \rho_2 \approx 4.0$ (red lines), $\alpha_3 = \rho_3 \approx 4.0$ (green lines). Similarly to the exponents of Δu , we find correspondence for the exponents of t with Euler's elastica for $n = 1$, and identical exponents for stress and strain, i.e., $\alpha_n = \rho_n$ —moreover, all numerical values for the exponents are consistent with half integers. In the remainder of this manuscript, we will fix the exponents α_n and ρ_n to their nearest integer values: $\alpha_1 = \rho_1 = 4$, $\alpha_1 = \rho_1 = 2$, $\alpha_2 = \rho_2 = 4$, and so on.

So far, we have determined the scaling exponents β_n , τ_n , α_n and ρ_n , but the post-buckling profile prefactors \bar{C}_n and \bar{D}_n remain to be determined. In fact, they simply follow from the fit of the data in Fig. 2.6(c) to Eqs. (2.14). For the most accurate determination of the prefactors, however, we refine our fit by using the fixed exponents α_n and ρ_n , and subsequently redo the fit. In Table 2.2 a summary of the prefactors \bar{C}_n and \bar{D}_n , as well as their ratios are given. Note that for the order $n = 1$, such values are in good agreement with those predicted by Euler's elastica for clamped-clamped boundary conditions.

n	\bar{C}_n	\bar{D}_n	\bar{C}_n/\bar{D}_n
0	72.0 ± 25	38.3 ± 13	1.88 ± 0.9
1	21.3 ± 3.2 $\left[\frac{4\pi^2}{\sqrt{3}} \approx 22.8 \right]$	21.1 ± 3.2 $\left[\frac{4\pi^2}{\sqrt{3}} \approx 22.8 \right]$	$1.01 \pm 0.2 [1]$
2	-116 ± 41	-553 ± 194	0.21 ± 0.1
3	320 ± 112	254.9 ± 89	1.26 ± 0.6
4	$-6.1 \cdot 10^3 \pm 2.4 \cdot 10^3$	$-1.4 \cdot 10^4 \pm 5.6 \cdot 10^3$	0.42 ± 0.2
5	$1.1 \cdot 10^4 \pm 5.5 \cdot 10^3$	$1.2 \cdot 10^4 \pm 6 \cdot 10^3$	0.99 ± 0.7

Table 2.2: Post-buckling profile prefactors \bar{C}_n and \bar{D}_n and their ratio, for the expansion of the nominal strain and stress profiles as defined by Eq. (2.11-2.12). Each row corresponds to a different order of n and values within the square brackets represent analytical results, predicted by Euler's elastica for clamped-clamped boundary conditions. The errors in the prefactors are an estimation, similar to the estimate made in Table 2.1. Here, however, the errors are larger than for the post-buckling profile exponents, because C_n and D_n follow from extrapolating our data up to $t = 1$ [Eqs. (2.14)]. Therefore, we estimate an error of 15% for $n = 1$, 35% for $n = 0, 2, 3$, 40% for $n = 4$ and 50% for $n = 5$.

Discussion

We have quantified how the nominal stress and strain profiles arise beyond buckling and observed intricate powerlaw scaling with the transversal coordinate x/w , beam width-to-length ratio t and post-buckling strain Δu :

$$\varepsilon\left(t, \Delta u, \frac{x}{w}\right) - \varepsilon_b = \sum_{n=0} \bar{C}_n t^{\alpha_n} \Delta u^{\beta_n} \left(\frac{x}{w}\right)^n, \quad (2.15a)$$

and

$$\frac{\sigma - \sigma_b}{E} \left(t, \Delta u, \frac{x}{w}\right) = \sum_{n=0} \bar{D}_n t^{\rho_n} \Delta u^{\tau_n} \left(\frac{x}{w}\right)^n. \quad (2.15b)$$

Our results in Table 2.1 indeed confirm that stress and strain share the same exponents in every order n , both in Δu and t . On the one hand, the scaling exponents for Δu of the nominal stress and strain equal 1 for even n , and 1/2 for odd n . On the other hand, the scaling exponents for t show that the linear order ($n = 1$) carries the lowest exponent in t , namely $\alpha_1 = \tau_1 = 2$, while the zeroth, quadratic and cubic order ($n = 0, 2, 3$) carry

a scaling exponent in t which equals 4 and the quartic and quintic orders ($n = 4, 5$) carry a higher scaling exponent in t of 6. We discuss further below how our results establish in detail the nonlinear corrections of the stress and strain profiles beyond the Euler limit.

Euler's limit, $O(t^2)$ — The dominant term of the asymptotic expansion given by Eqs. (2.15) is quadratic in t and corresponds to linear stress and strain profiles ($n = 1$, see Table 2.1), whereby the Euler's limit introduced in section 2.3.2 is recovered. This is further confirmed by the quantitative agreement between the measured and theoretical values of the post-buckling profile exponents and prefactors, that is, $\beta_1 \approx \tau_1 \approx 1/2$, $\alpha_1 \approx \rho_1 \approx 1/2$ [30] and $\bar{C}_1 \approx \bar{D}_1 \approx 4\pi^2/\sqrt{3}$. Note that as $\bar{C}_1/\bar{D}_1 \approx 1$, stress and strain are linearly related for $n = 1$, which confirms that linear elasticity is a correct approximation within Euler's limit.

Leading order nonlinear correction, $O(t^4)$ — The next contribution to Eqs. (2.15) is quartic in t and contains the zeroth, quadratic and cubic corrections in x/w to the stress and strain profiles ($n = 0, 2, 3$). A closer inspection of Table 2.2 reveals that, in contrast to $n = 1$, the post-buckling profile prefactors \bar{C}_n and \bar{D}_n are different. Because a linear constitutive relation would imply that Eq. (2.15a) and Eq. (2.15b) are equal, hence would have equal prefactors \bar{C}_n and \bar{D}_n , such a difference between the prefactors again evidences a nonlinear relation between stress and strain.

Next orders and convergence of the series expansion, $O(t^6)$ — Finally, we have carried out the fitting procedure up to sixth order in t and find that it involves the order $n = 4$ and $n = 5$ corrections in the stress and strain profiles. We have checked that for realistic values of beam width-to-length ratio ($t = 0.15$), these corrections are of relative magnitude $\lesssim 2\%$ and thus can be neglected. Therefore, in the remainder of the analysis we will neglect the orders $n \geq 4$, in other words, assume that the stress and strain profiles are accurately described by cubic polynomials.

2.4.3 Effective stress-strain law for the axial component

Above we argued that the difference between \bar{C}_n and \bar{D}_n evidences non-linearity in the stress-strain relation. In this section we set up the appro-

appropriate nonlinear stress-strain relation. Because the post-buckling slope [Eq. (2.2)] is defined in the vicinity of the buckling point, the starting point is to write a Taylor series for the normal stress around the buckling strain ε_b up to quadratic order, which yields

$$\sigma = \sigma_b + \left. \frac{\partial \sigma}{\partial \varepsilon} \right|_{\varepsilon=\varepsilon_b} (\varepsilon - \varepsilon_b) + \frac{1}{2} \left. \frac{\partial^2 \sigma}{\partial \varepsilon^2} \right|_{\varepsilon=\varepsilon_b} (\varepsilon - \varepsilon_b)^2 + \mathcal{O}(\varepsilon - \varepsilon_b)^3. \quad (2.16)$$

Defining the slope of the stress-strain curve at ε_b as an effective Young's modulus E_b , and the nonlinearity η as $\frac{1}{2} (\partial^2 \sigma / \partial \varepsilon^2)$, Eq. (2.16) can be written more compactly as

$$\frac{\sigma - \sigma_b}{E_b} = (\varepsilon - \varepsilon_b) + \eta (\varepsilon - \varepsilon_b)^2 + \mathcal{O}(\varepsilon - \varepsilon_b)^3. \quad (2.17)$$

We can calculate E_b and η analytically by evaluating the expansion in Eq. (2.16) using the stress-strain relation for uniaxially compressed neo-Hookean materials [Eq. (2.10a)]. This yields:

$$E_b(\varepsilon_b) = \frac{E}{3} \left(1 + \frac{2}{(1 + \varepsilon_b)^3} \right), \quad (2.18a)$$

and

$$\eta(\varepsilon_b) = -\frac{3}{2(1 + \varepsilon_b) + (1 + \varepsilon_b)^4}. \quad (2.18b)$$

Eqs. (2.18) show that as ε_b becomes increasingly negative, both the effective stiffness E_b and the magnitude of nonlinearity parameter η increase. In particular, we find, by expanding Eqs. (2.18) for small ε_b , that the leading order corrections to E_b and η are linear in ε_b :

$$E_b/E = 1 - 2\varepsilon_b + \mathcal{O}(\varepsilon_b^2), \quad (2.19a)$$

$$\eta = -1 + 2\varepsilon_b + \mathcal{O}(\varepsilon_b^2). \quad (2.19b)$$

Furthermore, note that as $\varepsilon_b \rightarrow 0$, we retrieve $E_b/E = 1$ and $\eta = -1$, in agreement with the small strain limit of uniaxially compressed neo-Hookean materials given by Eq. (2.10b). In the following, we will take the first order corrections to η and E for finite ε_b into account. However, we

will show in section 2.6.2 that these ε_b corrections are subdominant for our theoretical prediction of the post-buckling slope.

Our previous expansion of the strain and stress profiles, and our determination of the post-buckling profile prefactors \bar{C}_n and \bar{D}_n , provide a self-consistency check on the nonlinearity parameter η , detailed in the following. Using the scaling expressions given by Eq. (2.15), we can write the series expansion for the nominal strain, Eq. (2.15a), as:

$$\begin{aligned} \varepsilon(x) - \varepsilon_b &= \bar{C}_0 t^4 \Delta u + \bar{C}_1 t^2 \Delta u^{\frac{1}{2}} \left(\frac{x}{w}\right) + \bar{C}_2 t^4 \Delta u \left(\frac{x}{w}\right)^2 \\ &+ \bar{C}_3 t^4 \Delta u^{\frac{1}{2}} \left(\frac{x}{w}\right)^3 + \mathcal{O}\left(\left(\frac{x}{w}\right)^4\right). \end{aligned} \quad (2.20a)$$

Similarly, we can write the series expansion for the nominal stress [Eq. (2.15b)] as:

$$\begin{aligned} \frac{\sigma(x) - \sigma_b}{E} &= \bar{D}_0 t^4 \Delta u + \bar{D}_1 t^2 \Delta u^{\frac{1}{2}} \left(\frac{x}{w}\right) + \bar{D}_2 t^4 \Delta u \left(\frac{x}{w}\right)^2 \\ &+ \bar{D}_3 t^4 \Delta u^{\frac{1}{2}} \left(\frac{x}{w}\right)^3 + \mathcal{O}\left(\left(\frac{x}{w}\right)^4\right). \end{aligned} \quad (2.20b)$$

Substituting Eq. (2.20a) into Eq. (2.17) and comparing the post-buckling profile coefficients in each order of x with those of the proposed stress expansion of Eq. (2.20b), yields the following equalities in lowest order in Δu and t :

$$\bar{D}_0 = \bar{C}_0, \quad (2.21a)$$

$$\bar{D}_1 = \bar{C}_1, \quad (2.21b)$$

$$\bar{D}_2 = \bar{C}_2 + \eta \bar{C}_1^2, \quad (2.21c)$$

$$\bar{D}_3 = \bar{C}_3. \quad (2.21d)$$

The above equalities for the order $n = 0, 2, 3$ are consistent with the values of \bar{C}_1 and \bar{D}_1 in Table 2.2, within error bars, thus showing consistency with Eq. (2.17). Furthermore, the equality for $n = 2$, Eq. (2.21c), provides us with the following relation between C_n , D_n and η :

$$\eta = \frac{D_2 - C_2}{C_1^2}, \quad (2.22)$$

from which we then estimate, using Table 2.2, that $\eta \approx -1.0 \pm 0.6$. Though the deformations are not homogeneous in a buckled beam, we thus find that this indirect determination of η is consistent with the expected non-linearity parameter for homogeneous uniaxial compression of neo-Hookean materials, raising further hope that our expansion scheme is consistent and correct.

2.4.4 Series expansion of the nominal shear stress and strain

As we had seen earlier (Fig. 2.4), shear effects become substantial for wide beams—the nominal shear and compressive strains have the same magnitude for a beam of $t = 0.1$. In this section we therefore analyse in detail how the nominal shear strain and stress profiles evolve with (i) the beam's width-to-length ratio t , and (ii) the post-buckling displacement, Δu . We find that the nominal shear strain and stress profile evolve similarly with Δu and t , which implies a *linear* stress-strain relation for the shear.

We consider the shear profile at an inflection point of the beam ($x, s = \ell/4$), where the shear is maximal [see Fig. 2.4(c)]. We consider then the profiles $\gamma(x) \equiv \varepsilon_{xz}(x, s = \ell/4)$ and $\tau(x) \equiv \sigma_{xz}(x, s = \ell/4)$ to measure the spatial shape of the nominal strain and stress as a function of the scaled transverse coordinate x/w .

Polynomial expansion and asymptotic analysis

Following a similar series expansion as in Eqs. (2.11-2.12), we expand the nominal shear strain and stress profiles as:

$$\gamma\left(t, \Delta u, \frac{x}{w}\right) = \sum_{n=0} J_n(t, \Delta u) \left(\frac{x}{w}\right)^n, \quad (2.23a)$$

and

$$\frac{\tau}{G}\left(t, \Delta u, \frac{x}{w}\right) = \sum_{n=0} K_n(t, \Delta u) \left(\frac{x}{w}\right)^n, \quad (2.23b)$$

where J_n and K_n are the post-buckling profile coefficients of the expansion at order n . Note that prior to buckling, the beam simply undergoes uniform uniaxial compression and has not developed any curvature yet.

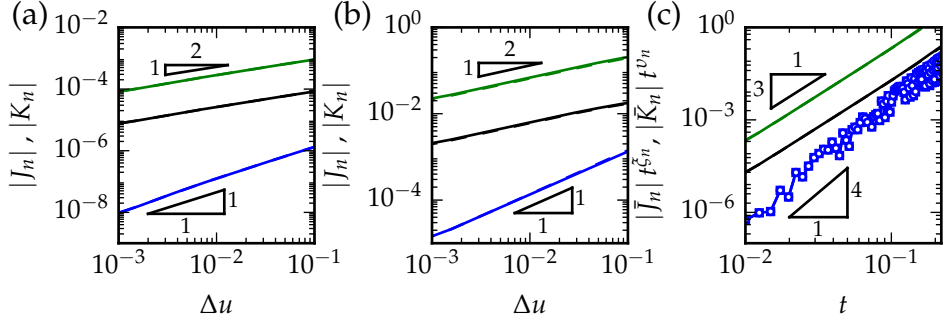


Figure 2.7: Dependence of the spatial nominal shear strain and stress profiles on Δu and t , obtained by FEM simulations. In black, blue and green we have plotted the post-buckling profile coefficients J_n (solid lines) and K_n (dashed lines), corresponding to order $n = 0$, $n = 1$ and $n = 2$ respectively. (a-b) We have plotted $|J_n|$ and $|K_n|$ as function of Δu for (a) a slender beam ($t = 0.02$) and (b) a thick beam ($t = 0.15$). (c) Dependence of J_n and K_n on the beam's aspect ratio t .

Therefore, unlike the uniaxial nominal strain and stress which are constant across the beam in the prebuckling regime, the shear stress and strain are strictly zero for $\Delta u \leq 0$.

Similarly to the post-buckling profile coefficients C_n and D_n [Eqs. (2.12)], we use that $J_n = K_n = 0$ at buckling, and we assume that the post-buckling profile coefficients J_n and K_n grow as power laws in t and Δu in the post-buckling regime:

$$J_n(t, \Delta u) = \bar{J}_n t^{\xi_n} \Delta u^{\Xi_n}, \quad (2.24a)$$

and

$$K_n(t, \Delta u) = \bar{K}_n t^{\nu_n} \Delta u^{Y_n}. \quad (2.24b)$$

Here, ξ_n , Ξ_n , ν_n and Y_n are the post-buckling profile scaling exponents, and \bar{J}_n and \bar{K}_n are the post-buckling profile prefactors which are yet to be determined from numerical simulations.

To determine all the constants, we use the same set of $N = 10^2$ FEM simulations as before, from which we now extract the spatial shape of the nominal shear stress and strain as function of x/w along a cross section at one quarter of the beam, $s = \ell/4$, and fit $\gamma(x)$ and $\tau(x)/G$ to polynomials of order $n = 3$. From the resulting fits we then obtain the post-buckling

n	Δu		t	
	Ξ_n	Y_n	ζ_n	v_n
0	0.49 ± 0.02	0.49 ± 0.02	3.02 ± 0.15	3.01 ± 0.15
1	1.03 ± 0.05	1.06 ± 0.05	3.98 ± 0.20	3.98 ± 0.20
2	0.50 ± 0.03	0.50 ± 0.03	3.02 ± 0.15	3.01 ± 0.15
3	1.02 ± 0.26	0.93 ± 0.23	5.93 ± 1.48	5.70 ± 1.43

Table 2.3: Post-buckling profile scaling exponents of Δu and t , for the expansion of the nominal shear strain and stress profiles as defined by Eqs. (2.23-2.24). Each row corresponds to a different order of n and results are provided up to cubic order ($n = 3$). We estimate the errors using the same arguments as in Table 2.1, and estimate an error of 5% for $n \leq 2$ and 25% for $n = 3$.

profile coefficients J_n and K_n for a specific set of parameter values t and Δu . From these quantities we subsequently deduce the post-buckling profile scaling exponents and prefactors up to order $n = 3$.

Fitting protocol — In Fig. 2.7 we plot $|J_n|$ (solid lines) and $|K_n|$ (dashed lines) as function of Δu and t , from which we observe power law behaviour in Δu and t . To determine the post-buckling profile scaling exponents and prefactors we perform the same fitting procedure as in the previous section and provide the results in Tables (2.3-2.4), up to $n = 3$. Note that Fig. 2.7 shows results up to $n = 2$ for clarity.

Results — First, note from Fig. 2.7 that the curves for the shear stress and strain coincide. Similarly, $\bar{J}_n/\bar{K}_n \approx 1$, and we conclude that a linear relation governs the leading order relation between nominal shear stress and strain. Second, we find that the post-buckling profile scaling exponents for Δu equal 1 for even n , and $1/2$ for odd n which is precisely opposite to the situation for the uniaxial nominal stress and strain exponents. Third, the scaling exponents for t show that the zeroth and quadratic order ($n = 0, 2$) together carry the lowest exponent in t , namely $\zeta_0 = \zeta_2 = v_0 = v_2 = 3$, followed by the linear order ($n = 1$) which scales as t^4 , and the cubic order ($n = 3$) which scales as t^6 .

n	\bar{J}_n	\bar{K}_n	\bar{J}_n/\bar{K}_n
0	-18.9 ± 1.9	-18.8 ± 1.9	1.0 ± 0.14
1	-45.3 ± 4.5	-45.3 ± 4.5	1.0 ± 0.14
2	205.9 ± 20.6	204.3 ± 20.4	1.0 ± 0.14
3	$-4.4 \cdot 10^3 \pm 1.8 \cdot 10^3$	$-3.7 \cdot 10^3 \pm 1.5 \cdot 10^3$	1.2 ± 0.68

Table 2.4: Post-buckling profile prefactors \bar{J}_n and \bar{K}_n and their ratio, for the expansion of the nominal shear strain and stress profiles as defined by Eqs. (2.23-2.24). Each row corresponds to a different order of n and results are provided up to cubic order ($n = 3$). Using the same arguments as in Table 2.2 we estimate an error of 10% for $n \leq 2$ and 40% for $n = 3$.

Discussion

We have quantified how the nominal shear stress and strain profiles arise beyond buckling and observed intricate powerlaw scaling with the transversal coordinate x/w , beam width-to-length ratio t and post-buckling strain Δu :

$$\gamma\left(t, \Delta u, \frac{x}{w}\right) = \sum_{n=0} \bar{J}_n t^{\xi_n} \Delta u^{\Xi_n} \left(\frac{x}{w}\right)^n, \quad (2.25a)$$

and

$$\frac{\tau}{G}\left(t, \Delta u, \frac{x}{w}\right) = \sum_{n=0} \bar{K}_n t^{v_n} \Delta u^{Y_n} \left(\frac{x}{w}\right)^n. \quad (2.25b)$$

First, we observe that the post-buckling profile exponents and prefactors of the expansions given by Eqs. (2.25) are equal (Table 2.4). Therefore, the nominal shear strain and stress are linearly related, hence we can assume

$$\tau(x) = G\gamma(x), \quad (2.26)$$

which is the result as predicted by [52] in the case of simple shear for neo-Hookean materials. We will use this linear constitutive equation for the shear in the remainder of this chapter.

Upon further inspection of the exponents in Table 2.4 we notice that the zeroth and quadratic order ($\sim t^3$) are dominant at small t . The linear order ($\sim t^4$) then serves as a first order correction to the shear profile, while the cubic order ($\sim t^6$) represents a higher order correction.

Timoshenko's limit, $\mathcal{O}(t^3)$ — The dominant terms within the expansions given by Eqs. (2.25) encompass both the polynomial order $n = 0$ and $n = 2$, which show the same scaling with t and Δu . The quadratic ($n = 2$) contribution to the nominal shear strain and stress is the strongest (Table 4). As a matter of fact, such a quadratic shear profile is in agreement with the textbook approach for the bending of linear elastic bars [100]. We will show later that this agreement is also quantitative.

Higher order corrections $\mathcal{O}(t^4)$ and convergence — The next contribution to Eqs. (2.25) is quartic in t and contains the linear correction to the shear stress and strain profiles ($n = 1$). We will take this term into account throughout the remainder of this manuscript. Lastly, to ensure the convergence of the asymptotic approach, we also carried out the expansion up to sixth order in t , and showed that it results in a cubic, negligible correction to the shear stress and strain profiles — for a beam with $t = 0.15$ and an $\Delta u = 0.1$, its relative magnitude is $\lesssim 1\%$.

In conclusion, we have developed a systematic expansion of the stress and strain profiles that allow us to capture the leading order effect of finite beam width for the post-buckling regime. This expansion involves terms of the form $t^p \Delta u^q (x/w)^n$, and we use our FEM simulations to determine the exponents p and q for the uniaxial and shear components of the strain and stress at each power n . This procedure circumvents the need for heuristics to guess the important terms, and leads to a greatly simplified model where the dominant next order terms in t are properly taken into account.

2.5 Energy density including material nonlinearity

In this section, we construct the 1D energy density which includes material nonlinearities, which come in two flavours. We first present the simplest version of the energy density, which has zero free parameters and does not need numerical input, and which is based on the combination of stress-strain nonlinearity and Mindlin-Reissner strains. The second version of the model takes corrections to the Mindlin-Reissner strains, such as Timoshenko's shear correction factor, into account, and it is this version that needs numerical input. Finally, this section ends with a discussion

of the physical interpretation of these corrections and a clear overview of the dominant next order terms in t and Δu to the energy density.

We start by expressing the total increase of the elastic energy beyond buckling. This increase follows from an integral of the respective products of stress and strain, integrated over the surface area of the beam, that is,

$$\begin{aligned} \mathcal{E}/d = \int ds dx \left(\int_0^{\varepsilon_{xx}} d\varepsilon'_{xx} \sigma_{xx} + \int_0^{\varepsilon_{yy}} d\varepsilon'_{yy} \sigma_{yy} + \int_{\varepsilon_b}^{\varepsilon_{zz}} d\varepsilon'_{zz} \sigma_{zz} \right. \\ \left. + \int_0^{\varepsilon_{xy}} d\varepsilon'_{xy} \sigma_{xy} + \int_0^{\varepsilon_{yz}} d\varepsilon'_{yz} \sigma_{yz} + \int_0^{\varepsilon_{xz}} d\varepsilon'_{xz} \sigma_{xz} \right). \end{aligned} \quad (2.27)$$

Even though we consider 2D beams, we keep a factor d (the depth) here to facilitate comparison to 3D beam results. For 2D beams, the ' yy ', ' xy ' and ' yz ' contributions are zero. Moreover, since the beam can freely expand along the x direction without any barrelling effects near the boundaries, we expect that $\sigma_{xx} \approx 0$ at each point of the beam, which we have verified numerically. As a result, we are left with the ' zz ' and ' xz ' terms, which correspond to the uniaxial and shear deformations, respectively.

Our aim is to set up an energy functional using the Mindlin-Reissner strains — 1D fields describing the shape of the beam along the curvilinear coordinate s . Therefore we define a linear energy density $\epsilon(s)$ as follows:

$$\mathcal{E} = \int_0^\ell ds \epsilon(s), \quad (2.28a)$$

where

$$\frac{\epsilon(s)}{d} = \int_{-\frac{w}{2}}^{\frac{w}{2}} dx \int_{\varepsilon_b}^{\varepsilon_{zz}(x)} \sigma(\varepsilon'_{zz}) d\varepsilon'_{zz} + \int_{-\frac{w}{2}}^{\frac{w}{2}} dx \int_{\varepsilon_b}^{\gamma(x)} \tau(\gamma') d\gamma'. \quad (2.28b)$$

Here, $\epsilon(s)$ represents the linear energy density that captures the amount of energy in a cross sectional area of the beam per unit length of the curvilinear coordinate s .

2.5.1 1D energy density without distortions

Here we present the energy density constructed from the Mindlin-Reissner strains without additional distortions. In that case, the nominal axial

and shear strain profiles across the beam equal $\varepsilon_{zz}(x) = \varepsilon_b + \varepsilon_0 + \varepsilon_1 x$ and $\varepsilon_{xz}(x) = \gamma_0$. We then evaluate the energy density in Eq. (2.28b) using these strain profiles in combination with the nonlinear axial stress-strain relation given by Eq. (2.17) and the linear shear stress-strain relation given by Eq. (2.26), and find that

$$\frac{\epsilon}{E_b} = A\varepsilon_b \varepsilon_0 + \frac{1}{2}A\varepsilon_0^2 + I \left(\frac{1}{2} + \eta \varepsilon_0 \right) \varepsilon_1^2 + \frac{GA}{2E_b} \gamma_0^2. \quad (2.29)$$

As can be seen from the above expression, the nonlinearity η introduces a coupling between the compressive strain ε_0 and the bending strain ε_1 , and such coupling is absent in previous, linear, beam models [42, 43]. The energy density given by Eq. (2.29) forms the basis of our nonlinear beam model we will derive in section 2.6, and, as mentioned above, this energy density has zero free parameters and therefore does not rely on numerical input.

2.5.2 1D energy density including distortions

We now present the energy density comprising distortions from the Mindlin-Reissner strains and built with the aid of numerical results. To this end, we substitute the respective stress-strain relations [Eq. (2.17) and Eq. (2.26)] in Eq. (2.28b) and carry out the integration with respect to the nominal strains ε_{zz} and γ . Second, we integrate with respect to x by using the expansions of the uniaxial and shear strain profiles up to cubic order [Eq. (2.15a) and Eq. (2.25a)]. This yields:

$$\begin{aligned} \frac{\epsilon}{E_b A} = & \left\{ \frac{\bar{C}_1^2}{24} \right\} \Delta u t^4 \\ & + \left\{ \frac{\bar{C}_1 \bar{C}_3}{80} + \bar{C}_0 \bar{C}_B + \frac{\bar{C}_2 \bar{C}_B}{12} + \frac{G}{E_b} \left(\frac{1}{2} \bar{J}_0^2 + \frac{1}{12} \bar{J}_0 \bar{J}_2 + \frac{1}{160} \bar{J}_2^2 \right) \right\} \Delta u t^6 \\ & + \left\{ \frac{\bar{C}_3^2}{896} + \left(\frac{\bar{C}_0^2}{2} + \frac{\bar{C}_0 \bar{C}_2}{12} + \frac{\bar{C}_2^2}{160} + \eta \frac{\bar{C}_0 \bar{C}_1^2}{12} + \eta \frac{\bar{C}_1^2 \bar{C}_2}{80} + \frac{G}{24 E_b} \bar{J}_1^2 \right) \Delta u \right\} \Delta u t^8 \\ & + \mathcal{O}(\Delta u^2 t^{10}). \end{aligned} \quad (2.30)$$

We have now carefully established the beam's energy density up to second order in excess strain and eighth order in the beam's width-to-length

ratio, $\mathcal{O}(\Delta u^2 t^8)$. The above analysis identifies and quantifies precisely how nonlinearity in the stress-strain laws and distortions to the Mindlin-Reissner kinematics alter the 1D energy density formulation. While the order $\mathcal{O}(\Delta u t^4)$ corresponds exactly to Euler's elastica, the order $\mathcal{O}(\Delta u t^6)$ comprises the classical Timoshenko beam contribution as well as distortions from the linear bending profile. The order $\mathcal{O}(\Delta u^2 t^8)$ contains the nonlinearity η as well as further distortions for bending and shear.

After a few manipulations which we explain hereafter, it can be shown that Eq. (2.30) can be converted in terms of the Mindlin-Reissner strains as:

$$\begin{aligned} \frac{\epsilon}{E_b} = A\epsilon_b \epsilon_0 + \frac{1}{2} A\zeta_2(\eta)\epsilon_0^2 + I \left(\frac{1}{2}\zeta_1(t) + \eta\epsilon_0 \right) \epsilon_1^2 \\ + \frac{GA}{2E_b} \gamma_0^2 (k_1 + k_2\gamma_0^2), \end{aligned} \quad (2.31a)$$

where the coefficients $\zeta_1(t)$ and $\zeta_2(\eta)$ are given by

$$\zeta_1(t) = 1 + 2 \left(\frac{\bar{C}_2 \bar{C}_B}{\bar{C}_1^2} + \frac{3}{20} \frac{\bar{C}_3}{\bar{C}_1} \right) t^2 + \frac{3}{112} \left(\frac{\bar{C}_3}{\bar{C}_1} \right)^2 t^4, \quad (2.31b)$$

$$\zeta_2(\eta) = 1 + \frac{1}{6} \frac{\bar{C}_2}{\bar{C}_0} \left(1 + \frac{3}{40} \frac{\bar{C}_2}{\bar{C}_0} + \frac{3}{20} \eta \frac{\bar{C}_1^2}{\bar{C}_0} \right), \quad (2.31c)$$

and where k_1 and k_2 are given by

$$k_1 = 1 + \frac{1}{6} \frac{\bar{J}_2}{\bar{J}_0} + \frac{1}{80} \left(\frac{\bar{J}_2}{\bar{J}_0} \right)^2, \quad (2.31d)$$

and

$$k_2(t) = \frac{1}{12} \frac{\bar{J}_1^2}{\bar{J}_0^4} t^{-4}. \quad (2.31e)$$

To obtain the above results we have used the fact that there is a clear pattern in the scaling exponents of the higher order corrections of the uniaxial and shear strain profiles with the excess displacement Δu , which alternate between 1/2 or 1 (see Tables 2.1 and 2.3). Consequently, we can factorize the Δu dependence and express the higher order corrections in terms of the Mindlin-Reissner strains. For example, the quadratic post-buckling profile coefficient of the axial strain profile, $C_2 = \bar{C}_2 \Delta u t^4$, can be expressed in terms of $\epsilon_0 \equiv C_0 = \bar{C}_0 \Delta u t^4$ as $C_2 = (\bar{C}_2/\bar{C}_0) \epsilon_0$.

2.5.3 Discussion

Here we discuss the physical interpretation of the corrections to the Mindlin-Reissner strains, and provide a clear overview of the dominant next order terms in t and Δu to the energy density.

Shear correction factors— Using Table 2.4, k_1 and k_2 can be evaluated as $k_1 = 0.67 \pm 0.15$ and $k_2(t) \approx 0.0013t^{-4}$. The constant k_1 is formally known as Timoshenko’s shear correction factor and our numerical value is in agreement with the value known in literature for beams with a rectangular cross section [102–104]. The shear correction factor accounts for the strongly quadratic, rather than uniform, shape of the shear profile across the beam [100]. This strong quadratic shape is also directly reflected by the data shown in Fig. 2.7, where the quadratic component is dominant over the zeroth and linear order component.

The quantity $k_2(t)$ corrects for the linear component of the shear strain profile and represents a higher order correction to the shear profile. Note that even though $k_2(t)$ is singular for $t \rightarrow 0$, $k_2(t)$ appears only within the product $k_2\gamma_0^4$ in Eq. (2.31a) (with $\gamma_0 \sim t^4$), such that the product $k_2\gamma_0^4$ is regularized for $t \rightarrow 0$.

Bending correction factors— Using Table 2.2, $\zeta_1(t)$ and $\zeta_2(\eta)$ can be evaluated as $\zeta_1(t) \approx 1 + 6(t^2 + t^4)$ and $\zeta_2(\eta) \approx 0.8 - 0.15\eta$. These quantities, which we refer to as bending corrections factors, describe the distortion of the linear strain profile, and thus take an analogous role as the shear correction factors described above, yet for bending. The mapping of energy contributions that arise from distortions of the linear strain profile onto the Mindlin-Reissner strains is one of the crucial aspects of this section.

Summary— We summarize our findings in Table 2.5: This clear analysis of the leading order terms and their relation to Timoshenko ($\mathcal{O}(\Delta u t^6)$) and Mindlin-Reissner ($\mathcal{O}(\Delta u^2 t^8)$) beam formulations is one of the key results of this work.

Model	Euler's Elastica	Timoshenko w/ bending correction	This work
Order	$\mathcal{O}(\Delta u t^4)$	$\mathcal{O}(\Delta u t^6)$	$\mathcal{O}(\Delta u^2 t^8)$
Terms	$1/2 I \varepsilon_1^2$	$1/2 I (\zeta_1(t) - 1 - \zeta_1'(t)) \varepsilon_1^2$ $+ A \varepsilon_b \varepsilon_0 + 1/2 G A k_1 \gamma_0^2 / E_b$	$I (\eta \varepsilon_0 + 1/2 I \zeta_1'(t)) \varepsilon_1^2$ $+ 1/2 A \zeta_2(\eta) \varepsilon_0^2$ $+ 1/2 G A k_2 \gamma_0^4 / E_b$

Table 2.5: Summary of the leading order terms in the expression of the (rescaled) linear energy density ε/E_b , extracted from Eqs. (2.30-2.31). We have defined $\zeta_1'(t) \equiv \frac{3}{112} \left(\frac{\bar{c}_3}{\bar{c}_1}\right)^2 t^4$ for convenience. While we recover exactly Euler's elastica at the order $\mathcal{O}(\Delta u t^4)$, our results suggest that Timoshenko's approximation requires a correction from the nonlinear bending profile at order $\mathcal{O}(\Delta u t^6)$. Moreover, this demonstrates that our work encompasses a higher order correction for the shear and a nonlinear correction for the stress-strain nonlinearity.

2.6 1D nonlinear beam model

In this section we formulate a 1D nonlinear model to describe the post-buckling of wide beams. Our model assumes (i) that the kinematics of the 1D model are captured by the Mindlin-Reissner strains, namely axial strain, curvature and shear [41]; (ii) that axial stress and strain are related nonlinearly. Based on these assumptions, we derive an expression for the 1D energy density as well as the governing equations for the mechanical equilibrium of wide beams. We then analytically solve the governing equations and find excellent agreement with 2D simulations for the post-buckling behaviour, without any adjustable parameters. Finally, we refine our beam model using extensive 2D simulations and show that distortions from Mindlin-Reissner kinematics have a negligible effect on the predictions by the model.

2.6.1 Mindlin-Reissner beam with a nonlinear stress-strain relation

Mindlin-Reissner kinematics describe beams that can be compressed, bent and sheared. These three deformation modes are quantified by a compressive $\tilde{\varepsilon}_0(s)$, curvature $\varepsilon_1(s) \equiv \theta_s(s)$ and shear strain $\gamma_0(s)$, as function

of the curvilinear coordinate s along the beam's central axis, with θ the deflection angle of the beam's axis with respect to the vertical. Therefore the total elastic energy of these beams is a functional of the form

$$\mathcal{E}[\tilde{\varepsilon}_0(s), \theta(s), \varepsilon_1(s), \gamma_0(s)] = \int_0^\ell ds \epsilon[s, \tilde{\varepsilon}_0(s), \theta(s), \varepsilon_1(s), \gamma_0(s)], \quad (2.32)$$

where the 1D energy density of the beam $\epsilon[s, \tilde{\varepsilon}_0(s), \theta(s), \varepsilon_1(s), \gamma_0(s)]$ exclusively depends on these strains.

The second key assumption is that stress and strain are related nonlinearly. To describe the vicinity of post-buckling, we set up an expansion of the nominal stress σ around the buckling strain ε_b up to quadratic order. This expansion, as derived already in section 2.4.3, yields

$$\frac{\sigma - \sigma_b}{E_b} = (\varepsilon - \varepsilon_b) + \eta(\varepsilon - \varepsilon_b)^2 + \mathcal{O}(\varepsilon - \varepsilon_b)^3, \quad (2.17)$$

where E_b and σ_b are the effective Young's modulus and nominal stress at buckling. In the case of neo-Hookean materials under plane stress conditions, the coefficients of this expansion can be determined analytically and read $\eta = -1 + \mathcal{O}(\varepsilon_b)$ and $E_b = E + \mathcal{O}(\varepsilon_b)$ (see section 2.4.3 for a demonstration). In the case of plane strain conditions, not considered here, it can be shown that $\eta = -3/2 + \mathcal{O}(\varepsilon_b)$ (see appendix 2.B.2). The nonlinearity of the above stress-strain relation stems from the combination of large deformations and incompressibility and can qualitatively be understood from the fact that upon compression (tension) the cross-sectional area increases (decreases) and the stress-strain curve is therefore effectively stiffening (softening). In addition, we assume a linear relation between the nominal shear stress τ and shear strain γ , $\tau = G\gamma$ in agreement with the elasticity of neo-Hookean materials [52].

Based on these two assumptions, we find that the 1D energy density describing post-buckling reads (see section 2.5):

$$\begin{aligned} \epsilon[\varepsilon_0(s), \varepsilon_1(s), \gamma_0(s)] &= E_b A \varepsilon_b \varepsilon_0 + \frac{1}{2} E_b A \varepsilon_0^2 \\ &+ E_b I \left(\frac{1}{2} + \eta \varepsilon_0 \right) \varepsilon_1^2 \\ &+ \frac{GA}{2} \gamma_0^2, \end{aligned} \quad (2.33)$$

with $\varepsilon_0(s) = \tilde{\varepsilon}_0(s) - \varepsilon_b$, $A = wd$ (the cross-sectional area) and G is the shear modulus. Note that the nonlinear correction proportional to η introduces a coupling between the compressive and bending strain, given by $\varepsilon_0\varepsilon_1^2$, and such coupling is absent in previous linear beam models [42, 43].

To establish the governing beam equations, the total elastic energy \mathcal{E} has to be minimized under the geometrical constraint set by the boundary conditions. In the case of Euler buckling, a uniaxial displacement is applied along the vertical axis of the beam and is associated to the following geometrical constraint:

$$\Pi = F \left(u - \left(\ell - \int_0^\ell ds \left((1 + \varepsilon_b + \varepsilon_0) \cos \theta - \gamma_0 \sin \theta \right) \right) \right), \quad (2.34)$$

where F is the Lagrange parameter associated with the axial displacement u that corresponds to the external axial force applied on the beam. We use the fact that $\varepsilon_1 \equiv \theta_s$ to apply the Euler-Lagrange formulation [105] on the energy functional including the constraint:

$$\tilde{\mathcal{E}}[\varepsilon_0(s), \theta(s), \varepsilon_1(s), \gamma_0(s)] = \int_0^\ell ds \varepsilon - \Pi, \quad (2.35)$$

which yields the governing equations of the beam:

$$E_b I \theta_{ss} + F \{ (1 + \varepsilon_b + \varepsilon_0) \sin \theta + \gamma_0 \cos \theta \} + 2\eta E_b I (\theta_s \varepsilon_0)_s = 0, \quad (2.36a)$$

$$F \cos \theta + E_b A (\varepsilon_b + \varepsilon_0) + \eta E_b I \theta_s^2 = 0, \quad (2.36b)$$

$$GA \gamma_0 - F \sin \theta = 0. \quad (2.36c)$$

This set of three coupled equations determine the beam's central axis in the post-buckling regime of wide beams. We will refer to this set of equations as the 1D *nonlinear* beam model, since it includes the nonlinearity η .

Please note that in the limit of linear materials ($\eta = 0$ and $E_b = E$), Eqs. (2.36) correspond to the equations for a shearable and extensible beam derived by [43]. If additionally the beam is assumed non-shearable, $\gamma_0(s) = 0$ and Eq. (2.36c) drops out, leaving us with a simpler model derived by [42]. Finally, for inextensible beams $\varepsilon_0(s) = \varepsilon_b = 0$, Eq. (2.36b) drops out, and we recover Euler's elastica $EI\theta_{ss} + F\sin\theta = 0$ [24]. Our beam model thus correctly captures all these linear models.

2.6.2 Solutions to the 1D nonlinear beam model

In this section we solve the 1D nonlinear beam model given by Eqs. (2.36) and show that the post-buckling slope is dramatically changed and the compressive Mindlin-Reissner strain significantly improved, when incorporating a nonlinearity η .

Dimensionless form

The results below will be presented in dimensionless form and we introduce the following dimensionless quantities:

$$\bar{s} = \frac{s}{\ell}; \quad \bar{F} = \frac{F\ell^2}{E_b I}; \quad \Lambda^{-2} = \frac{I}{A\ell^2}. \quad (2.37)$$

The quantities \bar{s} and \bar{F} represent the dimensionless curvilinear coordinate and force respectively, and $\Lambda \sim \ell/w$ can be recognized as the slenderness ratio [30]. Using the dimensionless quantities, the set of scaled beam equations that follows from Eqs. (2.36) reads:

$$\theta_{\bar{s}\bar{s}} + \bar{F} \{ (1 + \varepsilon_b + \varepsilon_0) \sin \theta + \gamma_0 \cos \theta \} + 2\eta (\theta_{\bar{s}} \varepsilon_0)_{\bar{s}} = 0, \quad (2.38a)$$

$$\varepsilon_0 = - (\bar{F} \Lambda^{-2} \cos \theta + \eta \Lambda^{-2} \theta_{\bar{s}}^2 - \varepsilon_b), \quad (2.38b)$$

$$\gamma_0 = \bar{F} \Lambda^{-2} \frac{E_b}{G} \sin(\theta). \quad (2.38c)$$

In the remainder of this chapter we drop the over-bars, unless if noted otherwise. For convenience, we additionally define:

$$r \equiv \frac{E_b}{G} = 2(1 + \nu) + \mathcal{O}(\varepsilon_b(t)), \quad (2.39)$$

where ν is the Poisson's ratio.

In Eqs. (2.38) we use Euler's prediction for ε_b that accurately describes the onset of buckling, even for wide beams [Fig. 2.2(a)]. Furthermore, all the parameters E_b , r and η can be determined theoretically to leading order in the beam width-to-length ratio t . In what follows we use these predictions as input parameters and solve Eqs. (2.38) to obtain a closed-form expression for the post-buckling slope as function of and to leading order in t .

Closed-form expression for the post-buckling slope as a function of t .

Here we derive our main result, namely the post-buckling slope as a function of beam width-to-length ratio t . In deriving the post-buckling slope, we are interested only in the mechanical response of the beam infinitesimally beyond buckling. Therefore, we only need to solve Eqs. (2.38) for small ($\theta(s) \ll 1$), yet nonlinear beam deflections. As a first step, we expand the governing beam equations up to the cubic order in θ , and substitute Eqs. (2.38b-2.38c) into Eq. (2.38a) to obtain:

$$\begin{aligned}
 0 = & \theta_{ss} \left(1 - 2\eta \left(F\Lambda^{-2} + \varepsilon_b \right) - 6\theta_s^2 \Lambda^{-2} \eta^2 \right) + \theta \left(F + (r-1) F^2 \Lambda^{-2} \right) \\
 & - \theta^3 \left(\frac{1}{6} F + \frac{2}{3} (r-1) F^2 \Lambda^{-2} \right) + \theta^5 \left(\frac{1}{12} F^2 \Lambda^{-2} (r-1) \right) \\
 & + \left(\theta^2 \theta_{ss} + \theta \theta_s^2 + \frac{1}{6} \theta^3 \theta_s^2 \right) F \Lambda^{-2} \eta.
 \end{aligned} \tag{2.40}$$

We now solve this expanded equation using a perturbative expansion that is consistent with the symmetry of Eq. (2.40), which only contains odd powers in θ , and that matches the imposed clamped-clamped boundary conditions, $\theta(0) = \theta(1) = 0$:

$$\theta(s) = \alpha \sin 2\pi s + \beta \sin 6\pi s. \tag{2.41}$$

Here, α and β physically correspond to the maximum deflection angle of the first and third harmonic of the Fourier series which describe the beam shape $\theta(s)$. To see how α and β are coupled, we substitute the perturbative expansion for $\theta(s)$ in Eq. (2.40). By collecting all terms proportional to $\sin(6\pi s)$, and setting the sum of their coefficients to zero, we found that β is coupled to a higher power of α , specifically $\beta \sim \alpha^3$. Therefore, since $\alpha \ll 1$, $\beta \ll \alpha$, and in the following we set $\beta = 0$.

Under the assumption $\beta = 0$, Eq. (2.40) leads to an explicit equation relating the force F to the deflection α . Expanding $F(\alpha)$ for small deflection α , yields the shape of the pitchfork bifurcation [106]:

$$F(\alpha, \Lambda, \eta, r) = F_c + \kappa \alpha^2 + \mathcal{O}(\alpha^4), \tag{2.42}$$

where κ is the curvature of the pitchfork. To connect this excess force to the axial displacement u , we establish the relation between the deflection

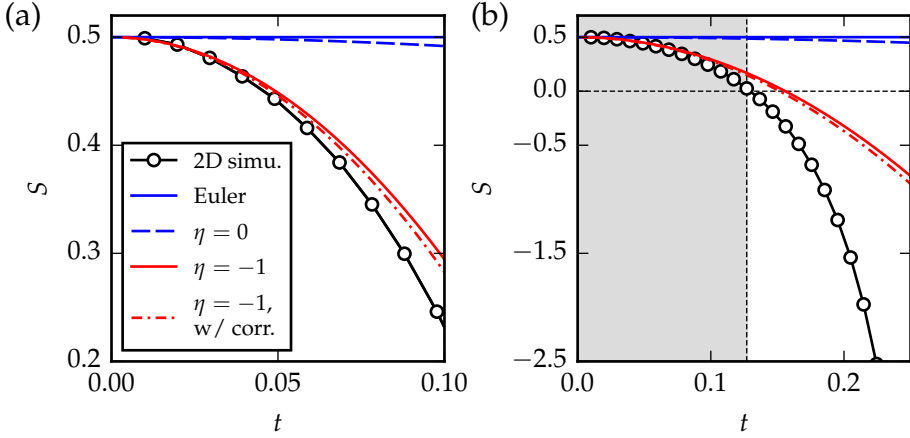


Figure 2.8: Post-buckling slope S as function of the beam width-to-length ratio t , for five different models. In the Euler limit $S = 1/2$, while in 2D simulations (open circles) S varies with t . Solutions to our model, given by Eq. (2.44), are shown for $\eta = 0$ (dashed blue) and $\eta = -1$ (solid red). Finally, we also show data for an extension of our model discussed in section 2.6.3 (dash-dotted red). (a-b) Panel (a) shows a close-up for $0 < t < 0.10$ and panel (b) shows a wider range of width-to-length ratio ($0 < t < 0.25$). The shaded region indicates the cross-over to subcritical buckling ($S < 0$) for the 2D simulations.

angle α and the axial displacement using the geometrical relation

$$u/\ell = 1 - \int_0^1 ds \{ (1 + \varepsilon_b + \varepsilon_0) \cos \theta - \gamma_0 \sin \theta \}, \quad (2.43)$$

which upon small deflections, can be expanded to obtain the desired relation $u(\alpha, F, \Lambda, \eta, r)$. We then invert this relation to $\alpha(u, F, \Lambda, \eta, r)$ and substitute it in Eq. (2.42), resulting in an equation that needs to be solved for $F(u, \Lambda, \eta, r)$. The final step is then to expand the solution for F in the limit $u \rightarrow u_c^+$, which leads to an equation of the form as in Eq. (2.2), with the post-buckling slope S equal to:

$$S = \frac{1}{2} - \left(\frac{1}{12} + 2\eta^2 \right) \pi^2 t^2 + \mathcal{O}(t^4). \quad (2.44)$$

This result confirms that Euler's elastica prediction ($S = 1/2$) is recovered in the limit of slender beams ($t \rightarrow 0$) and shows that the leading

order correction to the post-buckling slope S is quadratic in t . Notice that such correction comprises the stress-strain nonlinearity η . Does this correction bring an improvement for the prediction of the post-buckling slope? To check this, we compare the value of the post-buckling slope S obtained from 2D simulations to the prediction of Eq. (2.44), where the value of η is independently determined using the neo-Hookean model under the simplifying assumption that the neo-Hookean material is uniaxially compressed (see section 2.4.3). The comparison shown in Fig. 2.8 shows excellent agreement between the simulations and our prediction in Eq. (2.44), namely the quadratic correction matches the data very well for small t and remains accurate up to $t \approx 0.1$ [Fig. 2.8(a)]. Although we should not expect our prediction to be accurate for wider beams, it remains in qualitative agreement with the simulations and succeeds in predicting subcritical buckling at a critical width-to-length ratio $t \approx 0.15$ [Fig. 2.8(b)].

Beyond the success of our asymptotic approach, a closer inspection of the quadratic correction to the post-buckling slope S [Eq. (2.44)] allows us to infer three important conclusions. First, the quadratic correction is independent of the ratio of moduli r , given by Eq. (2.39). Since r sets the magnitude of shear deformations with respect to uniaxial compression, we conclude that shear is subdominant in the lowest order terms of $S(t)$. Second, the coefficient of the quadratic correction is quadratic in η [Eq. (2.44)], suggesting the sign of the nonlinearity does not play a role. This finding is consistent with earlier simulations and experiments on metabeams characterized by a positive nonlinearity ($\eta > 0$) [40], which similar to plain neo-Hookean beams ($\eta < 0$) were found to display a decreasing post-buckling slope as function of beam width. Third, the coefficient of the quadratic correction confirms our initial hypothesis that the stress-strain nonlinearity is the crucial ingredient to capture $S(t)$ correctly: The magnitude of this coefficient is entirely determined by the nonlinearity parameter η . In the absence of η the magnitude of the coefficient is much smaller, and $S(t)$ would be only weakly decreasing with t (see Fig. 2.8). We thus conclude that the nonlinearity η ensures that our theoretical prediction in Eq. (2.44) is able to capture the subcritical buckling at realistic aspect ratios, in contrast to earlier linear theories [41–43].

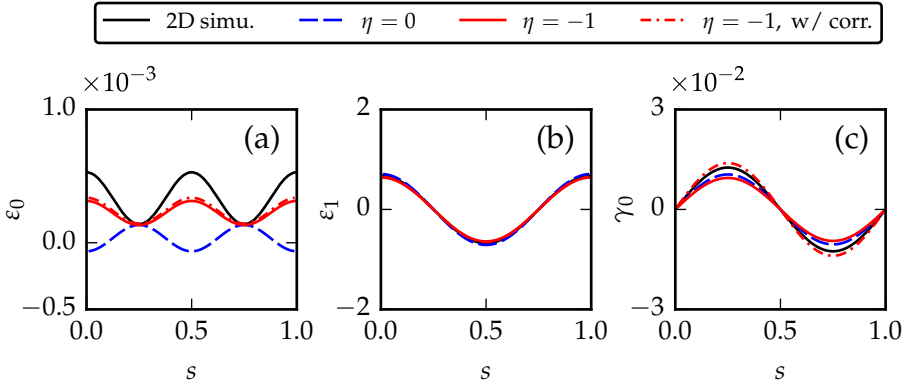


Figure 2.9: Mindlin-Reissner strains as a function of s , for four different models. We consider a wide ($t = 0.1$) beam which is compressed to an axial displacement of $u/u_c = 1.06$. We show results for 2D simulations (solid black), and compare them to numerical solutions to our beam model in Eqs. (2.38) for $\eta = 0$ (dashed blue) and $\eta = -1$ (solid red). Finally, we also show numerical solutions to an extension of our beam model in Eqs. (2.48) discussed in section 2.6.3 (dash-dotted red). (a-c) We have respectively plotted the compressive, bending and shear Mindlin-Reissner strain along the beam.

Mindlin-Reissner strains in the nonlinear beam model

We will now illustrate that the prediction for the compressive Mindlin-Reissner strain $\varepsilon_0(s)$ is significantly improved by the nonlinearity η . In Fig. 2.9(a-c) we plot the compressive, bending and shear Mindlin-Reissner strain for the 2D simulations and the beam model in Eqs. (2.38). First, panel (a) shows a significant qualitative difference in the Mindlin-Reissner strain $\varepsilon_0(s)$ between the linear and nonlinear beam model. In contrast to the linear beam model, the nonlinear beam model is in good qualitative agreement with the FEM simulations and the prefactors of the sinusoidal modulations all carry the same sign, albeit with a slightly smaller amplitude. This confirms our earlier assertion that the nonlinearity η is the crucial factor to capture correctly the large deformations of wide neo-Hookean beams. Finally, panel (b) and (c) show that the Mindlin-Reissner strains $\varepsilon_1(s)$ and $\gamma_0(s)$ remain essentially unchanged due to the nonlinearity and the model shows excellent agreement with the 2D simulations.

2.6.3 Distortions from Mindlin-Reissner kinematics with nonlinear stress-strain relation

The previous derivation of the 1D nonlinear beam model in Eqs. (2.38) is simple and directly follows from the use of two basic assumptions. In particular, using Mindlin-Reissner kinematics is a customary yet not controlled assumption. In this section, we investigate the validity of such a choice by using extensive numerical simulations and demonstrate that distortions from the Mindlin-Reissner kinematics systematically occur, modifying the 1D energy density and governing equations, albeit with a subdominant effect.

To explore deviations from Mindlin-Reissner strains, we have systematically investigated the stress and strain profiles in section 2.4. In particular, we find that the axial strain profile at the centre of the beam takes the form

$$\varepsilon(x) = \tilde{\varepsilon}_0 + \varepsilon_1 x + \varepsilon_2 x^2 + \varepsilon_3 x^3 + \dots, \quad (2.45)$$

where $x \in [-\frac{w}{2}, \frac{w}{2}]$ is the transverse coordinate across the beam width. Furthermore, $\tilde{\varepsilon}_0 = \varepsilon_b + \varepsilon_0$ and ε_1 are Mindlin-Reissner strains introduced in section 2.3, and ε_i (with $i \geq 2$) correspond to distortions from a linear axial strain profile. In section 2.4 we have also performed a similar systematic analysis for the shear profile.

Based on the extensive simulations and thorough asymptotic analysis procedure in sections (2.4-2.5), we found that the 1D energy density takes the form:

$$\begin{aligned} \epsilon[\varepsilon_0(s), \varepsilon_1(s), \gamma_0(s)] = & E_b A \varepsilon_b \varepsilon_0 + \frac{1}{2} E_b A (1 + \zeta_2(\eta)) \varepsilon_0^2 \\ & + E_b I \left(\frac{1}{2} (1 + \zeta_1(t)) + \eta \varepsilon_0 \right) \varepsilon_1^2 \\ & + \frac{GA}{2} \gamma_0^2 (k_1 + k_2 \gamma_0^2), \end{aligned} \quad (2.46)$$

where the coefficients E_b , η , $\zeta_1(t)$, $\zeta_2(\eta)$, G , k_1 and k_2 can be determined numerically. Note that in the limit when ζ_1, ζ_2 and k_2 are zero, we recover Eq. (2.33). Eq. (2.46) is very similar to Eq. (2.33) and the numerical values of the coefficients E_b , η , and G match the values that come from the neo-Hookean material model [52] (see section 2.4). In addition we see that the differences associated to distortions from the Mindlin-Reissner

kinematics can be captured by the coefficients $\zeta_1(t)$, $\zeta_2(\eta)$, k_1 and k_2 . While $k_1 = 0.67 \pm 0.15$ is a classical coefficient known as the shear correction factor [100, 102] whose value quantitatively matches Timoshenko's prediction [103, 104], $\zeta_1(t)$, $\zeta_2(\eta)$, and k_2 are undocumented and correspond to higher order distortions of the strain profiles. They have been determined in section 2.4 as:

$$\zeta_1(t) = 6(t^2 + t^4), \quad (2.47a)$$

$$\zeta_2(\eta) = -0.2 - 0.15\eta, \quad (2.47b)$$

$$k_2(t) = 0.0013t^{-4}. \quad (2.47c)$$

Note that even though $k_2(t)$ is singular for $t \rightarrow 0$, γ_0 scales as t^4 , such that the product $k_2\gamma_0^4$ that arises in Eq. (2.46) is regularized for $t \rightarrow 0$. Nonetheless, we see that the distortions in Eqs. (2.47) introduce minor modifications to the prefactors in Eq. (2.46) and in what follows we show that they do not play a major role in the model.

We now carry out the same Euler-Lagrange approach as previously and find the refined governing equations:

$$\zeta_1(t)E_bI\theta_{ss} + F\{(1 + \varepsilon_b + \varepsilon_0)\sin\theta + \gamma_0\cos\theta\} + 2\eta E_bI(\theta_s\varepsilon_0)_s = 0, \quad (2.48a)$$

$$F\cos\theta + E_bA(\varepsilon_b + \zeta_2(\eta)\varepsilon_0) + \eta E_bI\theta_s^2 = 0, \quad (2.48b)$$

$$GA\gamma_0(k_1 + 2k_2\gamma_0^2) - F\sin\theta = 0. \quad (2.48c)$$

This set of equations is the equivalent of the previously established beam equations [Eqs. (2.38)] and has been determined through a well defined and rigorous set of assumptions. Unfortunately, the coefficients $\zeta_1(t)$, $\zeta_2(\eta)$ and k_2 have to be determined numerically. Following the procedure in section 2.6.2 we linearise and solve Eqs. (2.48) and find that

$$S = \frac{1}{2} + \frac{(-3 + 2(1 + \zeta_2(\eta)) - 24\eta^2)\pi^2}{12(1 + \zeta_2(\eta))}t^2 + \mathcal{O}(t^4), \quad (2.49)$$

which reduces to Eq. (2.44) by setting $\zeta_2 = 1$. We have plotted Eq. (2.49) in Fig. 2.8 and see that the corrections ζ_1, ζ_2 and k_2 result in a minor improvement to the post-buckling prediction for S . Finally, we numerically solved Eqs. (2.48) to obtain the Mindlin-Reissner strains and plotted the result for $\eta = -1$ in Fig. 2.9. Again, we find that the corrections result in a

minor improvement to the post-buckling prediction, now for the Mindlin-Reissner strains. Altogether, this illustrates that the corrections ζ_1, ζ_2 and k_2 have a subdominant contribution to the post-buckling behaviour.

2.7 Conclusions and discussion

We have presented a thorough investigation of the post-buckling of nonlinear elastic beams, using experiments, finite element simulations and theory. In particular we have focussed on subcritical buckling, where, for neo-Hookean beams, the slope of the force-displacement curve becomes negative beyond buckling when the beam width-to-length ratio exceeds 12%. The main result of this chapter is a 1D nonlinear beam model that includes a material nonlinearity η . We constructed the model by building the beam's energy density using Mindlin-Reissner kinematics with a nonlinearity in the stress-strain relation, and demonstrated that this nonlinearity is crucial to accurately capture the post-buckling behaviour of wide beams and in particular to predict subcritical buckling. In contrast with previous works that have reported a significant effect of the ratio E/G on the flexure response [80] and the critical buckling force [43] of extensible and shearable beams, we found that E/G has a subdominant effect on the post-buckling slope.

Though our model has been established in the case of neo-Hookean material nonlinearity ($\eta < 0$), our findings could be generalized to a wider class of nonlinear elastic materials, such as cellular materials with nonlinear effective properties [21, 92, 107]. We expect this generalization to hold provided that the leading nonlinearity of the elastic material is quadratic in nature and that the material strains do not significantly deviate from the Mindlin-Reissner strain decomposition (as is shown in section 2.6.3 for 2D plane stress beams). For example, in recent work by [40], beams patterned with a periodic 2D pattern of pores were shown to exhibit positive, geometrically induced nonlinearity ($\eta > 0$). They found that a sufficiently strong nonlinearity leads to subcritical buckling, even when the beam width-to-length ratio is small. Such a transition to subcritical buckling for $\eta > 0$ is in qualitative agreement with our theory that predicts that the post-buckling slope essentially decreases quadratically in η with its maximum at $\eta = 0$ (Fig. 2.10). The present work rationalizes those findings and provide strong guidelines for the design of

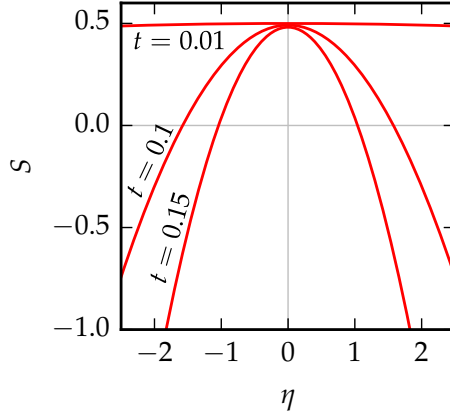


Figure 2.10: Post-buckling slope as a function of the nonlinearity η . Using Eq. (2.44) we have plotted $S(\eta)$ for $t = 0.01$, $t = 0.1$ and $t = 0.15$. The curves show that the post-buckling slope is quadratic in η and that the post-buckling slope does not exceed $S = 1/2$.

post-instability regimes in soft structures and metamaterials [108], where arbitrary values of η can be achieved [92]. We envision in particular that our description could be of interest for the design of compliant hierarchical cellular materials, which often rely on the buckling instability for their functionality [109, 110].

In addition, we note that other types of material nonlinearities could be explored and addressed within our framework, for instance, plasticity, stress-relaxation, swelling [111–115] or even growth and activity, which are ubiquitous in biological solids [116, 117]

Finally, while our work could be of great use for the engineering of systems that draw on Euler buckling for their functionality [36, 118], a plethora of compliant metamaterials harness the *snapping* instability [36, 44, 54, 58, 61, 119–122]. In order to understand the role of material nonlinearities on such instabilities and to devise mechanical design guidelines, our present framework should be generalized to pre-curved geometries, such as curved beams and shells.

2.A Numerical protocol for nonlinear buckling analysis

To determine the numerical force-displacement curve, we develop a two-step protocol. First, we perform a step-wise nonlinear stability analysis to approach the buckling displacement, u_c , with a relative accuracy of 10^{-3} . Such a step-wise nonlinear stability analysis consists of successive linear buckling analysis steps to take into account the change in beam geometry for large deformations. Subsequently, we perform an eigenfrequency analysis to determine numerically the proximity of the critical point.

Second, we probe the (stable) post-buckling branch for axial displacements $u > u_c$. One problem that arises in the FEM simulations, however, is that the beam will not automatically jump to one of the two new stable branches that occur once the compression of the initial configuration exceeds u_c : The beam's symmetry is retained even for $u > u_c$ and the beam remains on the unstable branch. One possibility to circumvent this problem would be to seed the initial configuration with imperfections that ensure that the beam selects one of the two stable post-buckling branches. A major drawback of this approach is that it destroys symmetry, hence unfolding the pitchfork bifurcation that underlies buckling, and consequently makes it impossible to study the post-buckling branch in the vicinity of the critical point. In this chapter we crucially need to be able to probe the post-buckling branch in the vicinity of the critical point; we investigate the buckling properties of beams down to a relative post-buckling displacement as small as 10^{-3} . To probe the post-buckling branch with high accuracy, we make use of a temporary transverse perturbation at the centre of the beam: Having obtained u_c from the nonlinear stability analysis, we compress the initial configuration up to $0.95u_c$. Next, we force the beam in the bifurcated, buckled state by subsequently applying the transverse perturbation, increasing the compression up to $1.05u_c$ and releasing the transverse perturbation again. We then further probe this particular post-buckling branch by the increase of the compressive displacement up to $u = 2u_c$. Finally, we smoothly decrease the axial displacement from $u = 2u_c$ back to $u = 0.95u_c$ from which we can precisely backtrack the post-buckling branch. Altogether, this protocol allows to determine the location of the instability and the post-buckling behavior with high accuracy.

2.B Nonlinear stiffening of hyper-elastic beams

In this appendix we demonstrate for a neo-Hookean material model how the leading nominal stress-strain nonlinearity, η , manifests itself in the pre-buckling regime for beams under (i) plane stress and (ii) plane strain conditions. The focus of our work presented in this chapter lies on plane stress conditions, but we also determine η for the plane strain case which could be used as a further generalization to our model given by Eqs. (2.38).

In the derivation below we consider a beam under uniaxial loading in the z -direction with its depth parallel to the y -axis [e.g. as in Fig. 2.1(a)], and allow for free lateral expansion at the boundaries unless noted otherwise. We then determine the leading nonlinearity η by expanding the axial nominal stress-strain relation $\sigma_{zz}(\varepsilon_{zz})$ for small strains as

$$\sigma_{zz}/E = \varepsilon_{zz} + \eta\varepsilon_{zz}^2 + \mathcal{O}(\varepsilon_{zz}^3), \quad (2.50)$$

where ε_{zz} and σ_{zz} are the vertical nominal strain and stress. Since the rubbers used in our experiments are well described by the incompressible formulation of nonlinear elasticity [93], we employ the strain energy density for an incompressible neo-Hookean material [52]

$$W = \frac{E}{6} (\lambda_1^2 + \lambda_2^2 + \lambda_3^2 - 3), \quad (2.51)$$

with E Young's modulus and λ_i the stretch in the principal direction $\hat{\mathbf{e}}_i$. The stretch λ is defined as the length ratio given by the length of a deformed line element to the length of the corresponding undeformed line element. Hence, $\lambda_i < 1$ expresses compression and $\lambda_i > 1$ extension of an element oriented along direction $\hat{\mathbf{e}}_i$. For an incompressible material the volume must remain unchanged under any deformation, which in terms of the principal stretches translates into the constraint $\lambda_1\lambda_2\lambda_3 = 1$. Enforcing the constraint with the aid of a Lagrange multiplier Π , the stress-stretch relation for an incompressible, isotropic neo-Hookean material may be expressed concisely in terms of the Cauchy stresses as [52]

$$\sigma_i^c = \lambda_i \frac{\partial W}{\partial \lambda_i} - \Pi, \quad (2.52)$$

with σ_i^c the Cauchy stress and Π the Lagrange multiplier. The principal Cauchy stresses are readily related to the principal nominal stresses σ_i

through

$$\sigma_i = \sigma_i^c / \lambda_i. \quad (2.53)$$

Now, in the pre-buckling regime deformations are spatially homogeneous, hence λ_i is constant and the principal directions $(\hat{\mathbf{e}}_1, \hat{\mathbf{e}}_2, \hat{\mathbf{e}}_3)$ coincide with the main axes $(\hat{\mathbf{e}}_x, \hat{\mathbf{e}}_y, \hat{\mathbf{e}}_z)$ for each material point in the beam. In that case, adopting $(\hat{\mathbf{e}}_x, \hat{\mathbf{e}}_y, \hat{\mathbf{e}}_z)$ as the new principal directions, λ_z simply relates to the vertical nominal strain ε_{zz} by

$$\lambda_z = 1 + \varepsilon_{zz}, \quad (2.54)$$

whereas Eq. (2.53) can be equally written as [52]

$$\sigma_{zz} = \sigma_z^c / \lambda_z. \quad (2.55)$$

Using these simplifications, the desired relation $\sigma_{zz}(\varepsilon_{zz})$ is readily obtained by calculating σ_z^c . Below we determine σ_z^c and distinguish between plane stress and plane strain conditions.

2.B.1 Plane stress

For plane stress conditions and free lateral expansion at the boundaries, the transverse stresses σ_x^c and σ_y^c must be zero. Therefore, evaluating Eq. (2.52) for the x and y component of the Cauchy stress provides us the constraint

$$\Pi = \frac{E}{3} \lambda_x^2 = \frac{E}{3} \lambda_y^2. \quad (2.56)$$

The above relation implies that $\lambda_x = \lambda_y$, as anticipated, and we proceed using λ_x as the independent stretch parameter. Having identified the constraint, the z component of the Cauchy stress follows as

$$\begin{aligned} \sigma_z^c &= \lambda_z \frac{\partial W}{\partial \lambda_z} - \Pi \\ &= \frac{E}{3} (\lambda_z^2 - \lambda_x^2) \end{aligned} \quad (2.57)$$

To express σ_z^c solely in terms of λ_z we combine the incompressibility condition $\lambda_x \lambda_y \lambda_z = 1$ with the relation $\lambda_x = \lambda_y$, and obtain $\lambda_x^2 = \lambda_z^{-1}$, so that

$$\sigma_z^c = \frac{E}{3} (\lambda_z^2 - \lambda_z^{-1}). \quad (2.58)$$

Finally, using the relations in Eqs. (2.54-2.55), we can write

$$\sigma_{zz} = \frac{E}{3} \left(1 + \varepsilon_{zz} - \frac{1}{(1 + \varepsilon_{zz})^2} \right), \quad (2.59)$$

which is the result as given by Eq. (2.10a). Expansion of the above equation for small ε_{zz} yields

$$\sigma_{zz}/E = \varepsilon_{zz} - \varepsilon_{zz}^2 + \mathcal{O}(\varepsilon_{zz}^3), \quad (2.60)$$

hence we conclude that $\eta = -1$ in the pre-buckling regime of beams under plane stress conditions.

2.B.2 Plane strain

In the plane stress case a beam has no deformations in the y -direction and no stresses in the x -direction, owing to the confinement in y -direction. Summarizing these conditions as $\sigma_x^c = 0$ and $\lambda_y = 1$, we identify the constraint as

$$\Pi = \lambda_x \frac{\partial W}{\partial \lambda_x}. \quad (2.61)$$

Therefore, the z component of the Cauchy stress equals

$$\begin{aligned} \sigma_z^c &= \lambda_z \frac{\partial W}{\partial \lambda_z} - \lambda_x \frac{\partial W}{\partial \lambda_x} \\ &= \frac{E}{3} (\lambda_z^2 - \lambda_x^2) \end{aligned} \quad (2.62)$$

To express σ_z^c solely in terms of λ_z we combine the incompressibility condition $\lambda_x \lambda_y \lambda_z = 1$ with the condition $\lambda_y = 1$, and obtain $\lambda_x = \lambda_z^{-1}$, so that

$$\sigma_z^c = \frac{E}{3} (\lambda_z^2 - \lambda_z^{-2}). \quad (2.63)$$

Following section 2.B.1, the above equation can be converted in terms of nominal stress and strain as

$$\sigma_{zz} = \frac{E}{3} \left(1 + \varepsilon_{zz} - \frac{1}{(1 + \varepsilon_{zz})^3} \right). \quad (2.64)$$

Note that the only difference with the result for plane stress in Eq. (2.59) is the exponent of the most right term. This exponent equals 3 for plane strain, but 2 for plane stress. Finally, expansion of Eq. (2.64) for small ε_{zz} yields

$$\sigma_{zz}/E = \frac{4}{3}\varepsilon_{zz} - 2\varepsilon_{zz}^2 + \mathcal{O}(\varepsilon_{zz}^3), \quad (2.65)$$

where the factor of 4/3 in front of ε_{zz} is introduced by the plane strain assumption — a beam supported on both sides is stiffer by a factor $1/(1 - \nu^2)$ [2]. Defining an effective Young's modulus $E' = E/(1 - \nu^2)$, the result in Eq. (2.66) can be rewritten as

$$\sigma_{zz}/E' = \varepsilon_{zz} - \frac{3}{2}\varepsilon_{zz}^2 + \mathcal{O}(\varepsilon_{zz}^3), \quad (2.66)$$

from which we conclude that $\eta = -3/2$ in the pre-buckling regime of beams under plane strain conditions.

